ELSEVIER

Contents lists available at ScienceDirect

International Journal of Mechanical Sciences

journal homepage: www.elsevier.com/locate/ijmecsci





Temporally continuous thermofluidic–thermomechanical modeling framework for metal additive manufacturing

Ritin Mathews ^{a,1}, Kishore Mysore Nagaraja ^a, Runyu Zhang ^a, Sumair Sunny ^a, Haoliang Yu ^a, Deon Marais ^b, Andrew Venter ^b, Wei Li ^a, Hongbing Lu ^a, Arif Malik ^{a,*}

- a Department of Mechanical Engineering, The University of Texas at Dallas, 800 W. Campbell Road, Richardson, 75080, TX, USA
- b Research and Innovation Division, The South African Nuclear Energy Corporation (Necsa) SOC Limited, Elias Motsoaledi Street Extension (Church Street West), R104 Pelindaba, Madibeng Municipality, 0240, North West Province, South Africa

ARTICLE INFO

Keywords: Directed energy deposition Additive manufacturing Computational fluid dynamics Finite element analysis Residual stress Neutron diffraction

ABSTRACT

Additive manufacturing (AM) is known to generate large magnitudes of residual stresses (RS) within builds due to steep and localized thermal gradients. In the current state of commercial AM technology, manufacturers generally perform heat treatments in effort to reduce the generated RS and its detrimental effects on part distortion and in-service failure. Computational models that effectively simulate the deposition process can provide valuable insights to improve RS distributions. Accordingly, it is common to employ Computational fluid dynamics (CFD) models or finite element (FE) models. While CFD can predict geometric and thermalfluid behavior, it cannot predict the structural response (e.g., stress-strain) behavior. On the other hand, an FE model can predict mechanical behavior, but it lacks the ability to predict geometric and fluid behavior. Thus, an effectively integrated thermofluidic-thermomechanical modeling framework that exploits the benefits of both techniques while avoiding their respective limitations can offer valuable predictive capability for AM processes. In contrast to previously published efforts, the work herein describes a one-way coupled CFD-FEA framework that abandons major simplifying assumptions, such as geometric steady-state conditions, the absence of material plasticity, and the lack of detailed RS evolution/accumulation during deposition, as well as insufficient validation of results. The presented framework is demonstrated for a directed energy deposition (DED) process, and experiments are performed to validate the predicted geometry and RS profile. Both single- and double-layer stainless steel 316L builds are considered. Geometric data is acquired via 3D optical surface scans and X-ray micro-computed tomography, and residual stress is measured using neutron diffraction (ND). Comparisons between the simulations and measurements reveal that the described CFD-FEA framework is effective in capturing the coupled thermomechanical and thermofluidic behaviors of the DED process. The methodology presented is extensible to other metal AM processes, including power bed fusion and wire-feed-based AM.

1. Introduction

It is well known that metal additive manufacturing (AM) induces high residual stresses (RS) within fabricated parts due to the steep thermal gradients, which contribute to excessive distortion and/or crack formation, resulting in large number of parts that fail to meet desired specifications [1–7]. The current state of AM technology, therefore, necessitates most manufacturing industries to oversize AM builds, perform heat-treatments to reduce the developed RS, and then apply conventional subtractive (machining) processes to achieve the desired final part attributes [8], especially in the aerospace industry [9–13].

With an aim towards improving AM processes, suitably formulated numerical models can help elucidate the underlying material behaviors that occur during deposition/melting/fusion that cannot be observed experimentally [14–17]. A more detailed technical understanding of AM processes, obtained through such improved prediction capability, can also lead to higher quality manufacturing and enhanced productivity [18–20]. Recent interests have also increased in optimizing build free-form topology and process specifications [21,22], as well as employing artificial intelligence and machine learning to AM [23–26].

Early numerical models of AM evolved from welding models [34], that exhibit similar geometric and thermal behavior during

E-mail address: arif.malik@utdallas.edu (A. Malik).

^{*} Corresponding author.

¹ Now with Oak Ridge National Laboratory.

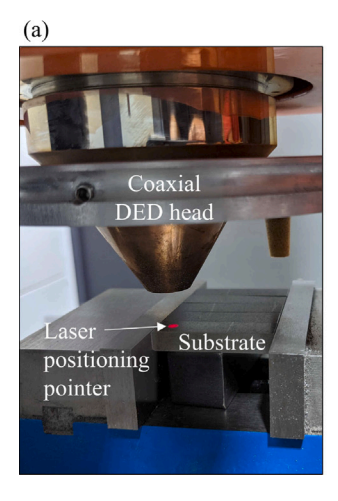
Table 1
Summary of relevant literature employing coupled thermofluidic-thermomechanical simulations of AM

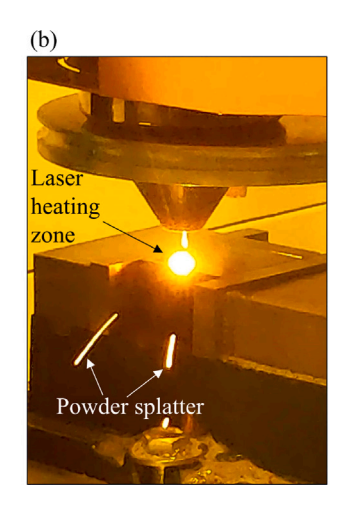
Authors (Year)	Summary of investigation, key findings, and simplifications relevant to present work
Jamshidinia et al. (2013) [27]	 Modeled electron beam melting AM process using a one-way coupled thermofluidic-thermomechanical technique to study the effects of beam scan speed on the thermal stress developed. Ti-6Al-4V was used as the material. Considered the effects of molten material flow. Thermal prediction from the CFD model was mapped on to the FEA model. Showed that stress evolves continuously due to non-uniform thermal evolution. Cooling rate was found to be the dominant parameter that influences the induced stress.
	 A simple, fixed rectangular geometry was used.
Cheon et al. (2016) [28]	 Modeled gas metal arc welding process to predict solid phase distribution due to variable cooling rates based on continuous cooling transformation diagram. AH36 steel was used as the material. Experimentally measured thermal data used to validate thermofluidic model. The final-time thermal profile from CFD simulation was mapped on to the FEA mesh to simulate cooling process and consequent material hardness. Discussed the importance of well calibrated thermal boundary conditions. RS developed during the deposition process was not studied.
Mukherjee et al. (2017) [29]	 A heat-transfer and fluid flow model was linked to Abaqus® FEA to predict RS. DED of Inconel 718 and Ti-6Al-4V were studied. Geometric evolution of the build was not considered. Temperature evolution was validated with experiments. The predicted RS was compared with published experimental measurements. Ti-6Al-4V component generated larger magnitudes of RS compared to Inconel 718. Layer thickness and laser heat input were found to influence RS development.
Bailey et al. (2017) [30]	 Laser direct deposition of H13 steel was modeled by coupling an in-house coded CFD technique with Abaqus® FEA. Geometry based validation of CFD model was performed. Investigated solid phase transformation and RS development. Results were validated against hardness measurements and X-ray diffraction RS measurements. Geometry evolution during the build was simplified using steady-state assumptions. Deactivated the melt-pool elements claiming they did not participate in RS development. Modeled a smaller simulation domain compared to experiment.
Chen and Yan (2020) [31]	 Modeled electron beam melting AM of Ti-6Al-4V using a one-way coupled thermofluidic-thermomechanical framework. Quiet element approach was employed in the thermo-mechanical simulation to capture geometry evolution resulting from the thermofluidic model. Results from the coupled framework were compared with FEA thermomechanical simulation to show agreement in RS prediction. Activation of elements at room temp resulted in unrealistic expansion of material during temperature mapping. Assumed linear elastic material behavior although predicted stress exceeds well beyond the yield strength of the material.
Beghini et al. (2021) [32]	 Simulated DED AM process of stainless steel (SS) 304L using a one-way coupled thermofluidic-thermomechanical method. A CFD-Level set technique considering all forms of heat transfer was employed to predict thermal behavior. CFD-FEA coupling was achieved by direct meshing and mapping algorithms. Considered effect of particle impingement. FE mesh conformed to the smooth geometry. Interpolation and mapping performed between CFD and FEA, as well as between each step of FEA. Comparison with pure thermomechanical model showed importance of geometry evolution in stress development.
Liang et al. (2021) [33]	 A laser-based wire feed AM of Ti-6Al-4V was modeled to analyze RS development via one-way coupled thermofluidic-thermomechanical model. The geometry evolution was captured by a custom meshing algorithm to reduce computational cost. Considered the effects of particle impingement. Concentration of stress was found at the center and towards the corners of the bead. Build geometry found to significantly influence stress magnitudes.

deposition/building process [35]. Finite element analysis (FEA) has been extensively used in the past to predict the evolution of RS and part distortion during and after the build. Hussein et al. [36] developed an FEA model to simulate a selective laser melting (SLM) process wherein a moving Gaussian distributed heat source was used to predict thermal behavior that was subsequently mapped into a mechanical model to

predict RS. A similar approach was followed by Farahmand and Kovacevic [37], wherein an X-ray diffraction RS measurement technique was employed to validate the model. In 2015, Heigel et al. [38] developed an improved formulation by applying Goldak et al.'s double ellipsoid heating model [39], combined with an element activation/deactivation technique to simulate a directed energy deposition (DED) process. Based on comparison with experimental RS measurement, it was found

observations.





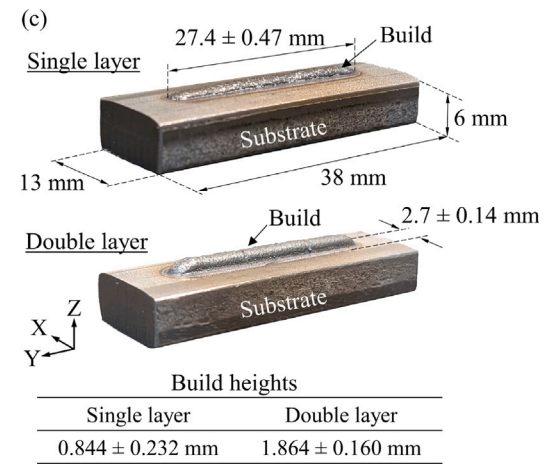


Fig. 1. (a) DED setup used to manufacture single- and double-layer samples. (b) DED AM deposition process. (c) Single- and double-layer printed specimens with dimensions. that well-calibrated thermal conditions were necessary for accurate RS prediction. Subsequently, similar approaches were employed to simulate electron beam melting [40], DED [41], and direct metal laser sintering [42]. In 2019, Li et al. [43] incorporated a mesh coarsening algorithm to this same type of approach to improve computational efficiency, while Tan et al. [44] considered phase change effects during the build to elucidate their influences on RS. Additionally, Nagaraja et al. in 2022 simulated the mitigation of tensile RS developed via DED by inducing compressive RS into the build using an ultrasonic nanocrystal surface modification technique [45]. Numerous other modeling efforts have been published previously to investigate metal deposition [46]. While the aforementioned finite element based studies were capable of predicting RS with sufficient accuracy, they lacked the ability to capture complex generic geometries as well as material behavior at high temperatures that aligns more closely with experimental data and

Significant developments in simulating the AM process have also been made by employing computational fluid dynamics (CFD), which is formulated to solve mass, momentum, and energy conservation equations. CFD has advantages in predicting rapidly evolving geometries that are accompanied by significant mass and heat transfer during the flow of molten material. Given the capability of CFD to account for fluid flow and phase changes, complex phenomena such as the Marangoni effect [47], balling, and denudation [48] can be predicted and accounted for during AM process simulations. Modeling the deposition of functionally graded material has also been demonstrated using CFD [49]. It has been shown that melt pool geometry and the corresponding heat transfer characteristics are sensitive to various factors [50,51]. To track and attain the free surface geometry in CFD models, either level set [52] or volume of fluid (VOF) [53] techniques are commonly used. The CFD - VOF technique has been demonstrated previously for both 2D and 3D AM models [54-56]. The CFD technique, however, lacks the ability to predict the mechanical response of the material, i.e., RS evolution and its effects on part distortion during the build process. Moreover, the overall thermomechanical and thermofluidic phenomena in AM are coupled, requiring their simultaneous (or at least pseudo-simultaneous) consideration. In light of this, a model that suitably couples the CFD and FEA physics can substantially improve the predictive capability. Table 1 summarizes the prior models and investigations aimed at coupling CFD and FEA for application to AM processes.

Although, as seen in Table 1, several publications involved frameworks that indeed couple the CFD and FEA formulations, the studies either lacked appropriate modeling techniques, resorted to simplifying assumptions, or neglected to include adequate validation of the results. For example, the research in [27,28,30] did not appropriately consider any temporally evolving geometry, while [28] describes a mapping of

the final-time thermal profile, obtained from CFD simulation, onto an FEA mesh to predict the residual stress during cooling, but it completely overlooked the RS evolution and accumulation taking place during the deposition process. Chen and Yan [31] assumed the material behavior to be purely elastic, thereby ignoring elastic-plastic behavior typically evident during cooling, even though the predicted stress in their work exceeded the yield strength of the material. Moreover, other than the work of Bailey et al. [30], none of those listed in Table 1 provide any comparison of their predicted RS to experimentally obtained results.

In light of the limitations of the prior studies, in this work a temporally-continuous, one-way coupled CFD-FEA model is developed to capture the thermofluidic and thermomechanical material behaviors, as it is applied to DED builds involving SS 316L material. Appropriately prescribed thermal boundary conditions, material constitutive model descriptions, and well-established mapping techniques (for temperature) are applied to overcome the limitations contained in the prior art. The predicted geometry and RS are subsequently compared with experimental measurements for validation. It is important to note that while a DED case study with SS 316L is included in this work, the demonstrated framework is extensible to other alloys and AM technologies such as electron beam melting, selective laser melting/sintering, etc.

Accordingly, the experimental work, which includes the DED process as well as the subsequent surface topography and RS measurements, is discussed in Section 2. Described in Section 3 is the one-way coupled thermofluidic-thermomechanical framework. A comparison of the demonstrated model's predictions with the experimentally acquired data is presented in Section 4. A summary of the work, and its findings, is given in the Conclusions in Section 5.

2. Experiment description

2.1. Directed energy deposition of SS 316L

Single- and a double-layer (bi-directional scan), single-bead DED builds with SS 316L are printed atop substrates of the same material (38 mm \times 13 mm \times 6 mm size), as shown in Fig. 1. The beads are approximately 27.4 mm long and 2.7 mm wide with measured bead heights of 0.84 mm and 1.86 mm, respectively.

The DED process is performed inside an enclosed chamber with a continuous flow of Argon carrier gas, that also provides the necessary shielding environment. A powder feed rate of 6 g/min of SS 316L particles that vary in size from 45 to 120 µm in diameter is supplied. For the first bead, a laser power of 600 W is applied, and for the second bead (double-layer build) the laser power is reduced to 300 W (to maintain similar thermal input compensating for heat accumulation from printing the first layer and to avoid unnecessary defects [49,57-59]). The laser scan speed is 127 mm/min (or 5 inch/min), with a spot diameter of 2 mm. Table 2 summarizes the DED process parameters.

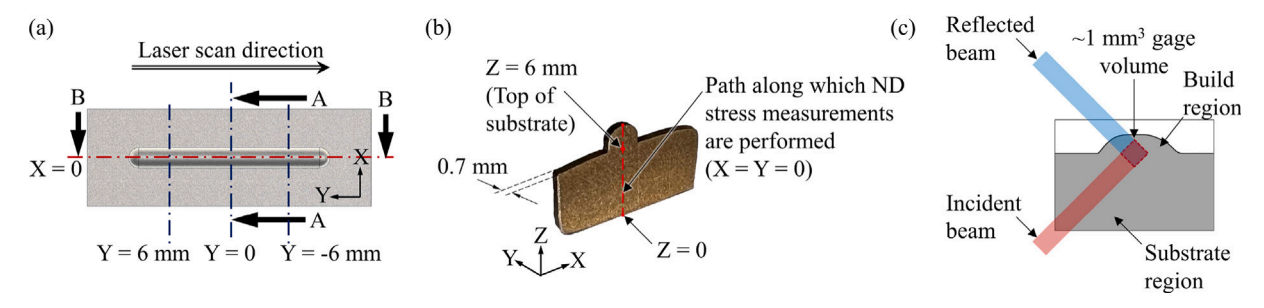


Fig. 2. (a) Depiction of longitudinal midplane (Section A-A) and transverse midplane (Section B-B) on a DED sample. (b) Photograph of the d_0 sample used in ND experiment to obtain stress-free lattice spacing, obtained at Section A-A. (c) Depiction of the incident and reflected beams in ND technique, showing the ~1 mm³ gage volume.

Table 2
Process parameters used for DED.

Parameter	Value
SS 316L powder particle diameter	45–120 μm
Powder feed rate	6 g/min
Laser power – 1st layer	600 W
Laser power – 2nd layer	300 W
Laser scan speed	127 mm/min
Laser spot diameter	2 mm
Bead length	27.4 mm

2.2. X-ray micro computed tomography and 3D surface topography scans

The build surface topography, of both specimens, is obtained using a 3D surface scanner (EinScan Pro 2X Plus) with a scanning accuracy of 40 μ m. To assess the presence of internal voids (or porosities) present within the builds, X-ray μ CT scans are performed on a Nikon C1 system with a scanning energy level of 185 kV at 62 μ A current, and a cubic voxel size of 17.947 μ m. 3D surface topography, acquired via the surface scanner, and cross-sectional images from the reconstructed μ CT scan are presented and discussed later in Section 4, Fig. 8, along with a comparison to the topography predicted by the demonstrated modeling framework. Additionally, the X-ray μ CT machine and cross-section images of the reconstructed μ CT results of the single- and double-layer builds are presented in the appendix of this article (Appendix A, Figs. A.19 and A.20).

2.3. Neutron diffraction residual stress measurement

To determine the residual stress developed due to the DED process, neutron diffraction (ND) measurements are performed at several locations within the build and substrate regions. The measurements are conducted on the MPISI neutron diffractometer at the SAFARI-1 research reactor. Venter et al. (2018) [60] provided details regarding the MPISI neutron diffractometer configuration parameters. The ND measurement setup utilizes a gage volume of approximately 1 mm 3 , shown in Fig. 2(c), to obtain diffraction patterns, which are subsequently used to measure lattice spacing, d. Consequently, the lattice spacing at a given measurement location is considered to be the average (or aggregate) value of atomic spacings within its respective gage volume.

A calibration sample, or d_0 sample as shown in Fig. 2(b), is obtained for each build configuration by extracting a 0.7 mm thick section, located approximately at the lengthwise center of the build, using wire electrical discharge machining (EDM) to mitigate cutting-induced effects that may influence the stress-free lattice spacing. Due to near plane-stress condition, the longitudinal (Y) component of stress in the d_0 samples will reduce to a negligible magnitude, thus enabling estimation of the stress-free lattice spacing, d_0 . Note that further reduction in thickness of the d_0 samples below 0.7 mm, while ideal to better emulate plane stress, was not performed so as to avoid excessive sample warpage that would impede measurement feasibility. Next, the stressed

and stress-free lattice spacings are used to calculate the local strain in the material, using Eq. (1).

$$\epsilon = \frac{d - d_0}{d_0},\tag{1}$$

where, ε is the strain, and $d-d_0$ represents the change in lattice spacing resulting from the presence of RS within the material.

Subsequently, local RS, σ , is calculated from the measured strains, ε , using Hooke's law, Eq. (2), where C is the stiffness coefficient. Further details on the measurement and calculations involved can be found in [61].

$$\sigma = C\varepsilon \tag{2}$$

RS measurements are performed at six locations along the intersection of X = 0 and Y = 0 planes, at Z = 0, 1 mm, 2 mm, 3 mm, 4 mm, 5 mm, and 6 mm, along the red dashed line path depicted in Fig. 2(b). Fig. 2(c) shows the upper-most measurement gage volume (centroid at Z = 6 mm) in the sample. It should be noted that while obtaining additional ND measurements of RS within the DED build region would be preferable, shifting the probed volume to a higher position than indicated would result in reduced signal quality, thus significantly increasing measurement error. In this work, RS at the various locations specified are obtained via two calibration approaches: (1) For each sample, a single unique d_0 value (obtained at Z = 1 mm on a substrate with no print) is used as the stress-free lattice spacing for all measurement locations (hereafter denoted as "unique d_0 "); (2) For each measurement location, the value obtained from the corresponding specific d_0 sample location is used as the stress-free lattice spacing (hereafter denoted as "specific d_0 "). Variation in RS between the two calibration approaches will help reveal any influence of chemical alteration within the material during deposition. The measured residual stresses for both single- and double-layer samples, plotted as a function of height, Z, are presented in Figs. 12 and 17. While the described measurements benefit from being a non-destructive process, and its ability to provide all three components of normal stress within the specimen depth, the process does have some drawbacks. Its usage requires complex and fragile equipment, the measurements are time-intensive, and error bands are relatively large compared to non-diffraction RS measurement techniques such as slitting.

3. Coupling the thermofluidic and thermomechanical formula-

This section describes the one-way coupling framework between the thermofluidic and thermomechanical models to simulate metal DED AM. The CFD-VOF simulation domain is initially set up based on the expected size of each printed specimen. DED process parameters (given in Table 2) and temperature-dependent thermofluidic material properties (obtained from [62] for SS 316L and summarized in Table 3) are incorporated. The thermofluidic solution is obtained using the Flow-3D solver [63].

The CFD-VOF model (shown in Fig. 3) consists of two rectangular domains, meshed with a grid resolution of 400 μm , stacked one on top

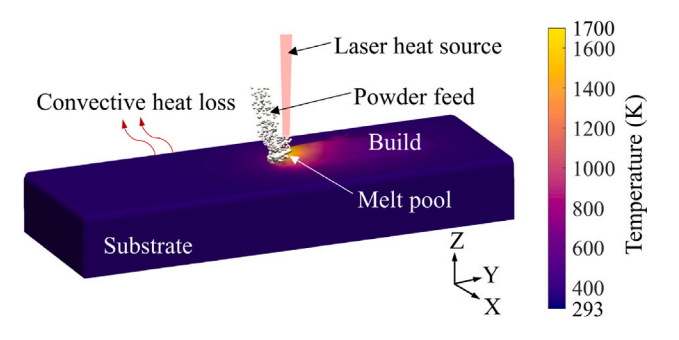


Fig. 3. CFD simulation of the single-layer sample, showing instantaneous temperature

of the other. The DED substrate is modeled as a fluid region within the bottom domain, with thermofluidic material properties of SS 316L assigned. The upper free surface of the substrate is located at the interface between the two domains. Thus, deposition occurs in the upper domain, which is initially defined as air at ambient temperature (293 K) and pressure (100 kPa). The side and bottom walls of the overall domain are constrained with symmetric boundary conditions. Material melting, layer formation, and solidification processes that occur during deposition are obtained by solving the mass, momentum, and energy conservation equations via the finite volume approach [64-66]. Additionally, the VOF technique [53] is used for tracking the interfaces between fluid states. In the CFD-VOF technique, each finite volume cell is assigned a scalar, time-dependent fluid fraction function, F, which holds a unique value between 0 and 1 for each fluid, and defines the overall state of the fluid in the cell. Note that the term "fluid" in this context is general and refers to a material definition that can be solid, liquid or gas, and/or different constituent material. A value of F = 1 represents a purely fluid region, while 0 represents a purely non-fluid region. Thus, any cell with a value lying between 0 and 1 must contain a fluid interface. The interface free surface is obtained by solving Eq. (3) for the largest variation of F, where t represents time, and v represents the velocity vector of the medium within the control

$$\frac{\partial F}{\partial t} + \nabla \cdot (vF) = 0 \tag{3}$$

Based on the value of F, the mass, momentum, and energy conservation equations (Eqs. (4)–(6)) are solved for each cell at each time step to obtain the thermofluidic solution.

$$\frac{\partial \rho}{\partial t} + \nabla \cdot (\rho v) = 0 \tag{4}$$

$$\frac{\partial}{\partial t}(\rho \mathbf{v}) + \nabla \cdot (\rho \mathbf{v} \otimes \mathbf{v}) = -\nabla p + \nabla \cdot (\mu \nabla \mathbf{v}) + \rho \mathbf{g} + \mathbf{f}$$
 (5)

$$\frac{\partial}{\partial t}(\rho h) + \nabla \cdot (\rho v h) + \dot{q} = \nabla \cdot k \nabla T \tag{6}$$

Here, ρ is the material density, p is the pressure, μ is the dynamic viscosity (specified as 0.08 g/cm-s), and g is the acceleration due to gravity. h represents the specific enthalpy, k is the thermal conductivity, T is the temperature, and \dot{q} is the heat flux rate. In the momentum equation, f represents the forces acting due to surface tension and Marangoni effects in the melt pool as described by Eq. (7) [67,68], given by,

$$f = \left[\gamma \kappa \mathbf{n} + \frac{d\gamma}{dt} (\nabla \mathbf{T} - \mathbf{n} (\mathbf{n} \cdot \nabla \mathbf{T})) \right] |\nabla F| \frac{2\rho}{\rho_{metal} + \rho_{gas}}, \tag{7}$$

where, γ is the surface tension, κ is the curvature, n is the surface normal vector, and ρ is the volume averaged density. The laser heat source is modeled as a Gaussian-distributed heat source. The amount of thermal energy induced, $\dot{q}_{\rm laser}$, at a given radial distance, r, from the laser spot center is given by Eq. (8).

$$\dot{q}_{\text{laser}}(\mathbf{r}) = \frac{\eta P_{\text{laser}}}{\pi R^2} e^{\left(-\frac{2r^2}{R^2}\right)},\tag{8}$$

Table 3
Temperature dependent material properties of SS 316L used in this work [62].

Property	Temperature (K)			
	293	1000	1500	2000
Thermal conductivity (W/m K)	12	25	32	20
Specific heat (J/kg K)	490	550	680	800
Coefficient of thermal expansion (×10 ⁻⁵)	1.5	1.8	2.1	2.1
Density (kg/m³)	7950	7650	7380	7380
Young's modulus (GPa)	200	150	80	50
Poisson's ratio	0.3	0.32	0.33	0.33

where, P_{laser} is the laser power, R is the laser spot radius, η is the absorptivity of the material (0.4 for the conditions in this work), which depends on the laser wavelength [69,70].

A powder source is defined at the starting point of deposition, from which a stream of particles of average size $100~\mu m$ at a rate of 2500 particles/s is introduced into the simulation domain, targeted towards the substrate surface. Nozzle geometry has been shown to influence powder flow behavior [71], albeit not considered in this work. The governing equation that defines the motion of particles is given by Eq. (9).

$$m_i \frac{d^2 x}{dt^2} = \mathbf{F}_{ij}^c + \mathbf{F}_i^f + \mathbf{F}_i^g \tag{9}$$

Here, m_i denotes the mass of particle i, x denotes the translational displacement vector, F_{ij}^c represents the contact force acting on particle i by another particle j, or a wall. F_i^f represents the drag force due to carrier gas flow, and F_i^g represents the gravitational force acting on the particle, given by Eqs. (10) and (11).

$$F_i^f = m_i \frac{18\mu_{gas}}{\rho_p d_p^2} \frac{C_D R_e}{24} (\mathbf{u} - \mathbf{u}_p)$$
 (10)

$$F_i^g = m_i \frac{g(\rho_p - \rho_g)}{\rho_*},\tag{11}$$

where, μ_{gas} , u, and R_e , are respectively the viscosity, velocity vector, and Reynold's number of the gas flow, C_D is the drag coefficient, u_p , ρ_p , and d_p are the velocity, density, and diameter of the particle, respectively. g is the acceleration due to gravity and ρ_g is the density of the carrier gas.

Since direct *in-situ* temperature measurements during the printing process were not performed due to equipment availability (e.g., high-temperature thermocouple or infrared camera), the geometry of the final build, obtained via 3D surface scans and volumetric images from the reconstructed μ CT scan, is used as reference for calibration and validation. The combination of both 3D surface scans and X-ray μ CT scans provides accurate external geometry for model calibration, as well as information on any voids/porosities present within the build. Molten material flow behavior in the computational model depends on gravity, buoyancy, Marangoni effects, surface tension, recoil pressure, and vaporization. Heat transfer modes of conduction, convection, and radiation are tuned, along with recoil pressure and vaporization since they influence the geometric and thermal prediction. Moreover, the CFD grid requires sufficient refinement to accurately capture the evolving geometry.

Once a predicted CFD build geometry of reasonable agreement with experimental data is obtained, the time-dependent geometric (G_t) and thermal (Th_t) dataset is exported for use in the FE thermomechanical model. The thermomechanical model is initially set up using a surrogate mesh that encompasses the entire build-substrate region (as depicted in Fig. 4). Temperature dependent material properties are applied for SS 316L [72–74] and the initial state of stress is specified as $\sigma_0=0$ MPa. Two initial thermal conditions are specified: (1) All nodes within the substrate are set to ambient temperature, (2) All nodes within the material deposition region (above the substrate) are set to material melting temperature (1700 K for SS 316L); before deactivating the elements located within the build region. Note that these initial conditions are overwritten with temperature boundary conditions as

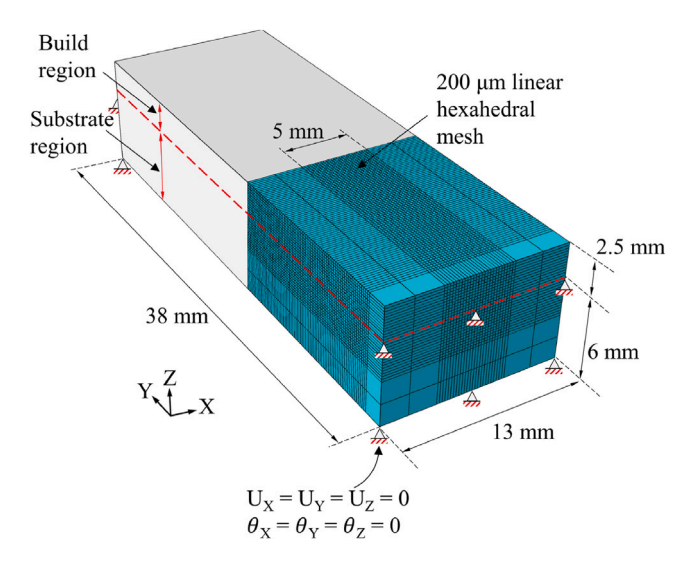


Fig. 4. Discretization of the thermomechanical model, showing boundary conditions.

the simulation progresses. Once the time loop is initiated, at each time step, the instantaneous geometric and thermal data (G_t and Th_t) are read from the CFD data. Elements instantaneously located within the printed geometry are activated while elements that lie outside the build geometry and those that lie within the melt pool are simultaneously deactivated. Note that elements within the melt pool are also deactivated for two reasons: (1) Material in molten state (liquid region) does not significantly participate in stress development in the solidified region (although shear forces, viscosity, and weight of liquid can plausibly have minor influences on stress, it is deemed negligible compared to the far more significant thermal effects). (2) From a simulation convergence perspective, since liquid material cannot withstand deviatoric stress (neglecting viscosity), the elements in the melt pool are unrealistically "soft" (as determined by the temperature-dependent Johnson–Cook flow stress material model); this can result in divergence of the solution, as even small forces acting on the molten material can result in excessively large deformation. Hence, for computational feasibility, yet with negligible adverse effects, deactivation of melt-pool elements is incorporated. Additionally, the active nodes are assigned temperature boundary conditions (replacing the initial temperature of 1700 K) based on a natural neighbor interpolation technique [75] using Th, obtained from the thermofluidic model at the particular instant in time. This methodology of specifying an initial temperature before activation, followed by temperature assignment immediately during activation assures that there is no unrealistic material expansion due to change in temperature from ambient to deposition temperature that influences RS. The thermomechanical solution is then obtained for that time step.

Each time step in the FE thermomechanical model imports the geometric (G_t) and thermal (Th_t) data obtained from the thermofluidic model for the equivalent time step in order to predict the RS developed due to thermal-mechanical behavior of the material during deposition and subsequent cooling. The build volume in the thermomechanical model is discretized using linear, full integration hexahedral elements with a mesh as fine as 200 µm. Note that the mesh is actually quite coarse relative to the size of the build, with around 20 elements along the width and 5 elements along the height, but given that the elements are of full integration formulation, the presence of 8 integration points within each element allows for step-wise variation of stress between 40 points along the width and 10 points along the height. A mesh sensitivity analysis is conducted to study the variation of stress distribution and magnitude with respect to element size via a simplified simulation for the same geometry described above. Herein, no element activation/deactivation is considered. Instead, all nodes above the substrate are initially set to 1700 K and all nodes within

the substrate are set to 293 K. The specimen is then allowed to attain thermal equilibrium considering ambient surroundings. The simulation is performed with elements of size 2000 μ m, 800 μ m, 400 μ m, 200 μ m, and 100 μ m. Fig. 5(a) shows the variation of longitudinal stress with respect to element size, after the sample attains thermal equilibrium. The stress profile converges as it reaches 100 μ m. On the other hand, Fig. 5(b) shows that the computational time increases exponentially as element size decreases.

Hence, 200 µm mesh is deemed sufficiently dense to capture the variation of stress through the build while balancing computational time. The mesh encompasses the substrate and build regions, represented by $[E_S]$ and $[E_B]$ respectively, with rigid boundary conditions (zero translations, $U_{X,Y,Z=0}$ and rotations, $\theta_{X,Y,Z}=0$) applied to planes Y=0 and Y=38 mm of the substrate (Eq. (12)), replicating those seen earlier in Fig. 1(a). Each node in the domain has one temperature and six displacement degrees of freedom.

$$\begin{array}{l} U_X=U_Y=U_Z=0 \\ \theta_X=\theta_Y=\theta_Z=0 \end{array} \right\} \ \forall \ nodes \ \in Y=0, \ Y=38 \ mm, \& \ Z \ \leq \ 6 \ mm \ (12) \\ \end{array}$$

Thermal boundary conditions represented by Eqs. (13) and (14) are implemented at the initial time step.

$$T = T_{\text{melt}} \ \forall \ \text{nodes} \ \in [E_B]$$
 (13)

$$T = T_{ambient} \ \forall \ nodes \in [E_S]$$
 (14)

A coupled temperature–displacement solution is obtained at every time step using the quasi-static solver of Abaqus 6.14. The thermomechanical model computes the Cauchy's stress tensor, σ_t , at each time step in accordance with 3D Hooke's law per Eq. (15).

$$\sigma_{t} = C : \varepsilon_{t}^{e} \tag{15}$$

$$\varepsilon_{t} = \varepsilon_{t}^{e} + \varepsilon_{t}^{pl} + \varepsilon_{t}^{T} + \varepsilon_{t-1}$$
(16)

$$\varepsilon_t^{\mathrm{T}} = \alpha(\mathrm{T}_t - \mathrm{T}_{t-1}),\tag{17}$$

where, C is the material stiffness tensor, and ε_t represents the total strain in the current time step. ε^e , ε^{pl} are respectively the elastic and plastic strains, ε^T is the thermal strain, T_t and T_{t-1} are the current and previous temperatures respectively, and ε_{t-1} denotes the total strain from the previous step. Material plasticity is modeled via the Johnson–Cook flow stress equation, given by Eq. (18)

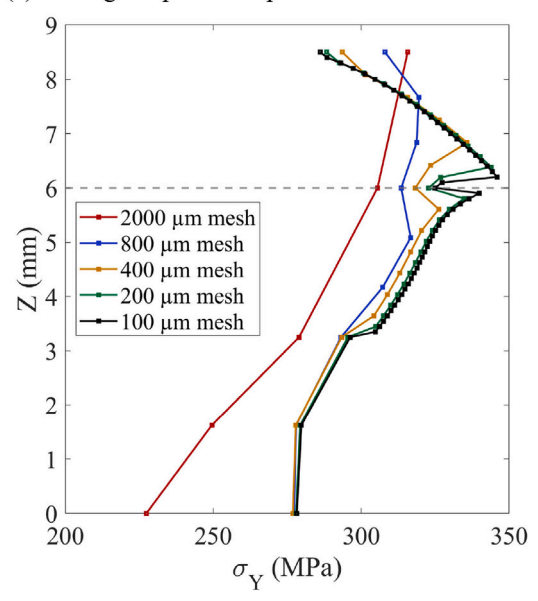
$$\sigma_{\rm f} = \left[A + B(\varepsilon^{\rm pl})^{\rm n} \right] \left[1 + C \ln \left(\frac{\dot{\varepsilon}^{\rm pl}}{\dot{\varepsilon}_{\rm 0}} \right) \right] \left[1 - \left(T^* \right)^{\rm m} \right], \tag{18}$$

where A is the quasi-static yield strength of the bulk material at room temperature, B is the strain hardening modulus, and C is the strain-rate hardening coefficient. $\epsilon^{\rm pl}$, $\dot{\epsilon}^{\rm pl}$, and $\dot{\epsilon}_0$ are the plastic strain, plastic strain rate, and the reference strain rate, respectively. n is the work-hardening exponent, m is the thermal softening exponent, and T^* is the nondimensional temperature term given by Eq. (19), normalized between the ambient temperature, T_0 , and the melting temperature of the material, $T_{\rm m}$.

Johnson–Cook plasticity model parameters obtained from milling tests conducted by Chandrasekaran et al. [74] are summarized in Table 4. $T_{\rm m}$ is specified as 2000 K instead of 1700 K (melting temperature of SS 316L [72]) to avoid numerical divergence caused by excessive distortion of elements located within the near-molten material, that are too "soft" to sustain deviatoric stress in the thermomechanical model. These elements, contrary to melt-pool elements, participate in stress evolution and cannot be deactivated.

$$T^* = \begin{cases} 0 & T_{t \le T_0} \\ \left(\frac{T_{t - T_0}}{T_{m - T_0}}\right) & T_0 < T_t < T_m \\ 1 & T_t \ge T_m \end{cases}$$
 (19)

(a) Through-depth stress profile



(b) Computational time

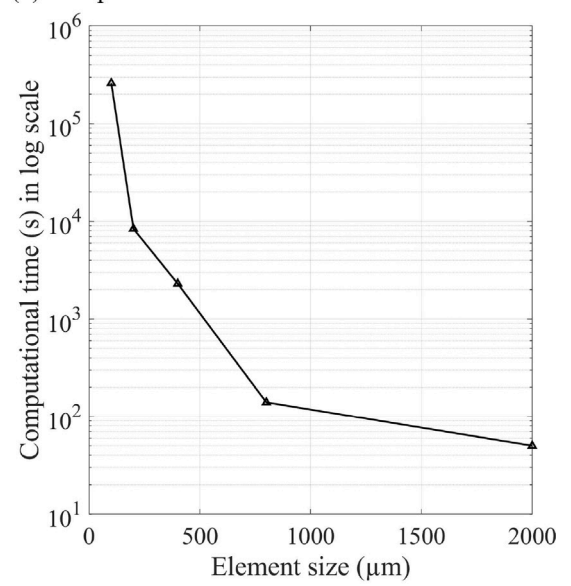


Fig. 5. (a) Convergence of longitudinal stress profile through the depth of sample. (b) Computational time plotted as a function of element size.

Table 4
Johnson–Cook flow stress model parameters used in the thermomechanical model [74].

Parameter	Value
A	305 MPa
В	1161 MPa
n	0.61
C	0.01
$\dot{\varepsilon_0}$	$1 s^{-1}$
T_0	293 K
$T_{\rm m}$	2000 K
m	0.517

The thermomechanical solution at each time step converges once the stress equilibrium conditions, described by Eqs. (20)–(22), are satisfied.

$$\nabla \cdot \sigma = 0 \tag{20}$$

$$\sigma \cdot \mathbf{n} = \mathbf{0}$$
 on free surface Γ (21)

$$\sigma = \sigma^{\mathrm{T}} \tag{22}$$

Subsequent time steps are simulated following the same procedure until the build is complete. The predicted stress and distortion results at any time step influence those predicted in the subsequent time steps, resulting in a continuously evolving stress state that is coupled to the thermal and geometric evolution. As mentioned, to validate the predicted stress field, a comparison is made with the RS data acquired via ND measurements.

The overall computational framework that couples the thermofluidic and thermomechanical solutions to predict geometric, thermal, and mechanical evolution during the AM process is summarized in the flowchart shown in Fig. 6. The coupling algorithm is achieved via Matlab programming and Python scripting between the two software platforms. The results obtained from the described one-way coupled model and their comparisons with experiments are discussed next.

4. Results and discussion

The thermofluidic model predicts the geometric and thermal distribution evolution of the build during deposition. Fig. 7 shows the

molten region and thermal distribution along the transverse cross section (section plane parallel to Section A-A in Fig. 2(a)) at the center of the melt pool, at time, t=3 s. A value of 1 on the melt region scale represents material in liquid state and a value of 0 represents material in the solid state. A value of 0.2 is assumed to be the mushy region threshold. Note that although the melting point of SS 316L is 1700 K, the mushy zone extends below the 1700 K isotherm and well into the substrate top surface, enabling a good bond.

The build surface topography acquired via the optical 3D surface scan and the X-ray μ CT scans is used to study variations between experimentally acquired data and geometry predicted via the thermofluidic model. In particular, note that for height of the single-layer build, as seen in Fig. 8(a) and (b), as well as with regard to the cross-sectional areas illustrated in Fig. 8 (c–e), subtle variations are observed. Fig. 8 (c–e) offer qualitative comparisons of the deposited bead's cross-sectional "dome shape" at three longitudinal locations (Y = -6 mm, Y = 0, Y = 6 mm; refer Fig. 2(a)).

A quantitative comparison of cross-sectional areas for the same is presented in Table 5. Comparing the prediction with the experimental data, note that maximum variations of about 24% and 16% are observed at section Y = 6 mm based on the 3D surface scan and Xray μ CT, respectively. This is actually due to a non-uniformity in the physical cross-section wherein for the initial few millimeters along the length, the build is physically smaller as compared to the middle and latter-deposited regions, as evidenced in Table 5. The effect likely arises as the result of a delayed build-up of powder flow through the nozzle and/or possible inconsistencies in carrier gas flow rate. In the thermofluidic model, however, variations in build cross-section are relatively indiscernible, since the material flow rate is assigned a preset value. Accordingly, sections at Y = -6 mm and Y = 0 are more representative for comparison and validation indicating an average variation of 4.12% from the 3D scan and 5.17% from the μ CT. Additionally, note that there is a net average variation of 5.2% between the 3D scan and µCT results between all three sections, indicating some inconsistency between the scanning technologies. Whilst these variations may quantitatively appear quite small, when observing the actual "dome shape" of the bead (see Fig. 8 (c-e)), subtle differences in geometry are evident. These can be attributed to one or more of several sources of measurement error during the scanning process; incorrect reference point calibration, temperature variations that influence the optical sensor characteristics, and software errors for the 3D surface

Table 5 Comparison of cross-sectional areas between the thermofluidic (CFD) prediction, 3D surface scan, and the X-ray μ CT at three transverse sections.

	CFD prediction (mm ²)	3D scan (mm²) [% Variation]	X-ray μCT (mm²) [% Variation]	% Variation 3D scan vs. X-ray μCT
Section $Y = -6 \text{ mm}$	2.136	2.230 [4.40]	2.31 [8.01]	3.46
Section $Y = 0$	2.104	2.023 [3.85]	2.055 [2.34]	1.57
Section $Y = 6 \text{ mm}$	2.176	1.654 [23.99]	1.83 [15.97]	10.56

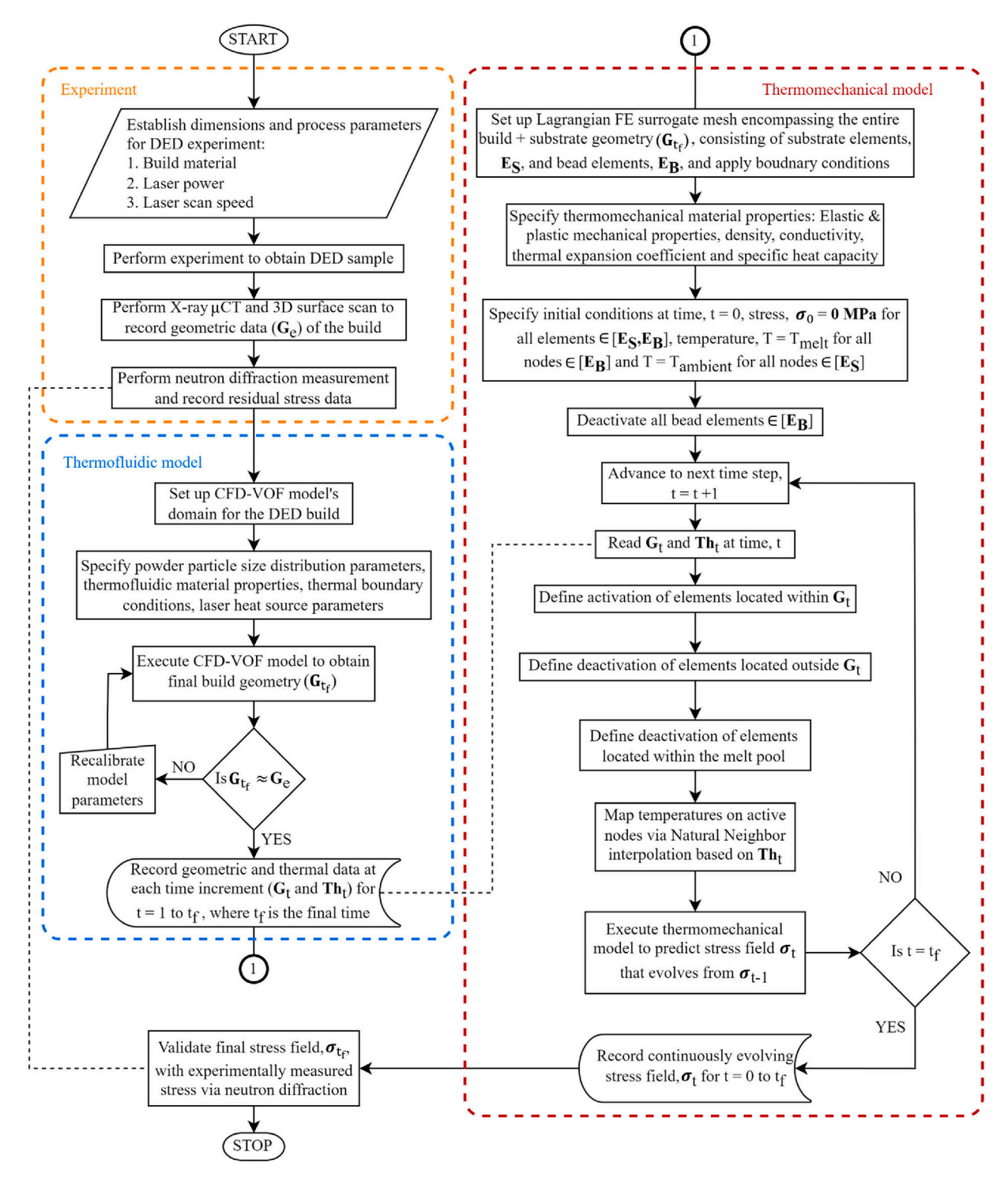


Fig. 6. Flowchart of the one-way coupled thermofluidic-thermomechanical framework introduced in this work.

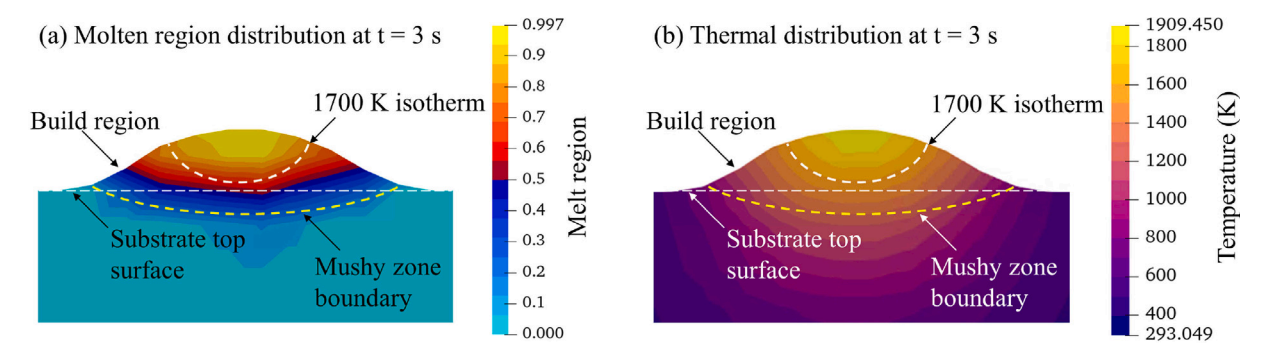


Fig. 7. (a) Depiction of molten region in the thermofluidic simulation during deposition of the first layer at time, t = 3 s. (b) Corresponding thermal distribution at the same instant. Note that the mushy zone extends below the 1700 K isotherm.

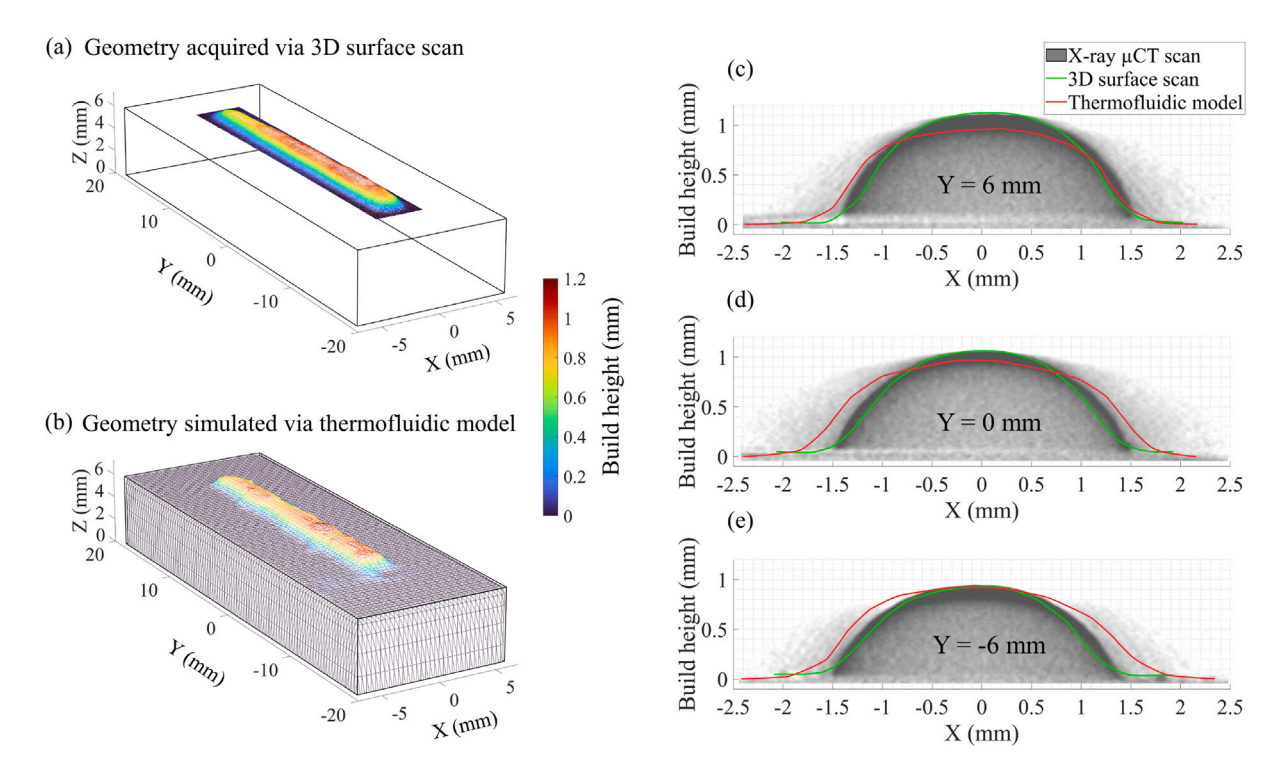


Fig. 8. Comparison of (a) experimentally obtained build geometry (via 3D surface scan), and (b) computationally predicted build geometry (via CFD), for the single-layer sample. (c-e) Comparison of cross-section areas obtained via X-ray μ CT, 3D surface scan, and thermofluidic prediction for three sections at Y = 6 mm, Y = 0, Y = -6 mm; refer Fig. 2.

scanner can result in inaccurate results [76]. On the other hand, μCT scanning is a relatively sensitive process where small movements in the lightweight sample during rotation of the platform, under-sampling, erroneous definition of the rotation axis, and contamination of the detector surface can result in false artifacts during reconstruction. Conebeam geometry defects are also an implicit source of error in the CT process [77].

For the single-layer build, temperature distribution along the transverse midplane, i.e., X=0 (or Section B-B in Fig. 2(a)), at a specific time frame (half way through the printing process at t=5.6~s) in the thermofluidic simulation, as well as the corresponding spatially interpolated and mapped temperature field in the thermomechanical simulation, are shown in Fig. 9(a). Enlarged isometric views of the melt pool in both simulations are presented in Fig. 9(b). The indentation near the melt-pool region in the thermomechanical model, Fig. 9(b) (bottom), is due to the elements that are part of the melt pool at that particular instant being deactivated for reasons stated earlier.

The spatial distribution of von Mises stress predicted at the end of the single-layer build along the longitudinal and transverse midplanes is presented in Fig. 10. The peak RS at the build-substrate interface is predicted to be \sim 450 MPa. At regions far from the build, the model

predicts significantly lower magnitudes of RS, as expected, due to relatively lesser heat penetration and accumulation. The framework also predicts variations in the magnitude and distribution of RS at the build-substrate interface along the length of the deposition. To better understand the RS distribution within the build and substrate regions, a quantitative comparison of the transverse and longitudinal normal components of RS plotted along multiple linear paths on the transverse midplane (X = 0), spanning the length of the build and substrate, as well as the depth of the build and substrate, is presented in Fig. 11.

The predicted transverse (X) and longitudinal (Y) components of RS, $\sigma_{\rm X}$ and $\sigma_{\rm Y}$ respectively, extracted on the transverse midplane (Section **B-B**, or X = 0), along three horizontal paths (Z = 4.5 mm, 5.5 mm, and 6.5 mm), and a vertical path (Y = 0) are plotted in Fig. 11. In agreement with existing research [36], the peak tensile stress $\sigma_{\rm Y}$ (~420 MPa) is much greater than the peak tensile stress $\sigma_{\rm X}$ (~150 MPa), as observed when comparing Fig. 11(b) and (c). This is because the laser scan considered in this work runs along the longitudinal direction. A similar observation can be made by comparing Fig. 11(d) with (e); The peak and average tensile stresses for $\sigma_{\rm Y}$ along the length of the build at different depths (Z) are predicted to be greater than that of stress

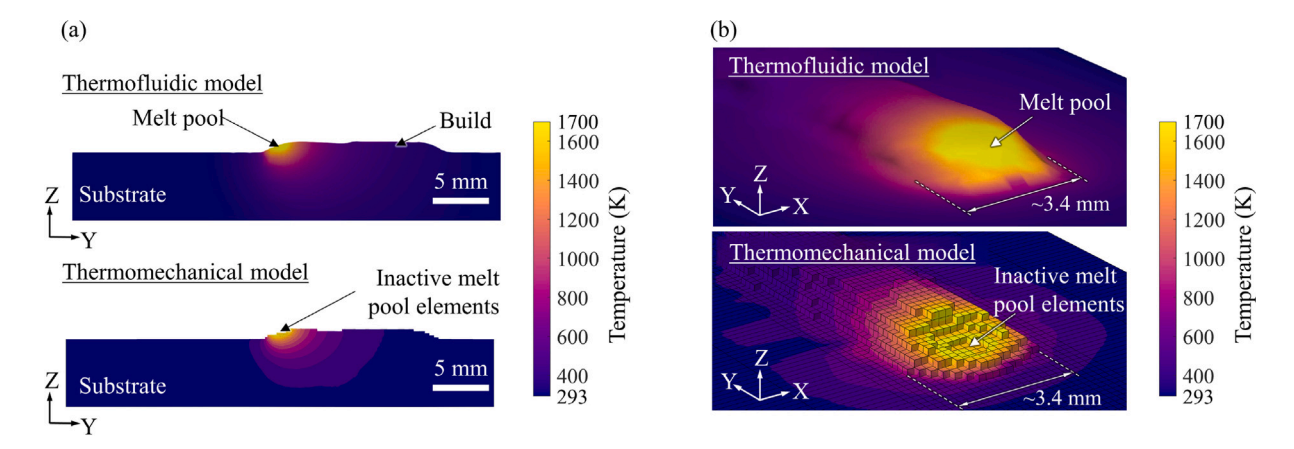


Fig. 9. (a) Comparison of thermal prediction along the longitudinal cross-section (Section B-B) from the thermofluidic model (top) during the DED process and the interpolated thermal solution from the thermomechanical model (bottom) at the equivalent time step. (b) Enlarged isometric view of the melt-pool region from the thermofluidic model (top) and from the thermomechanical model (bottom), showing the absence of melt-pool elements.

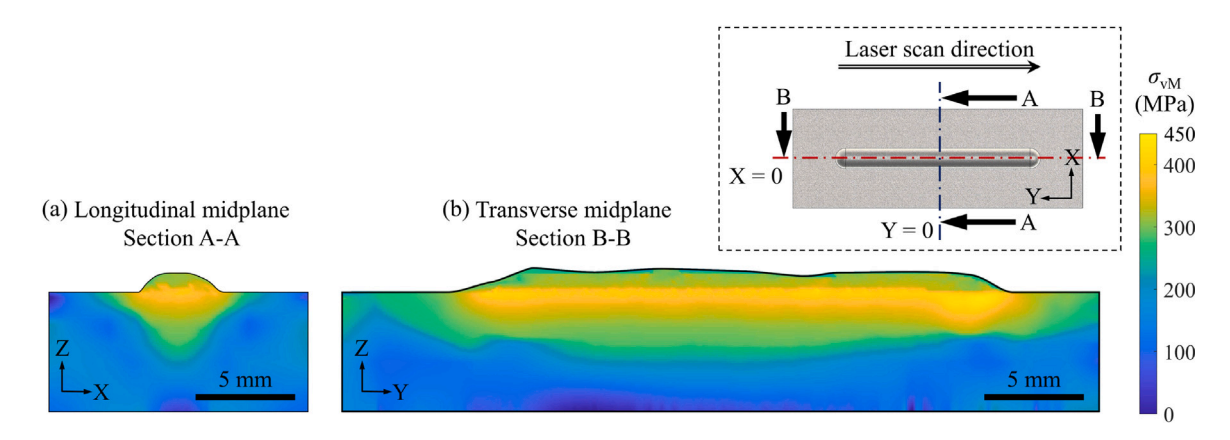


Fig. 10. von-Mises stress spatial distribution predicted at the end of deposition of the first layer along the longitudinal and transverse midplanes. Inset plot depicts Section A-A and B-B on a DED sample.

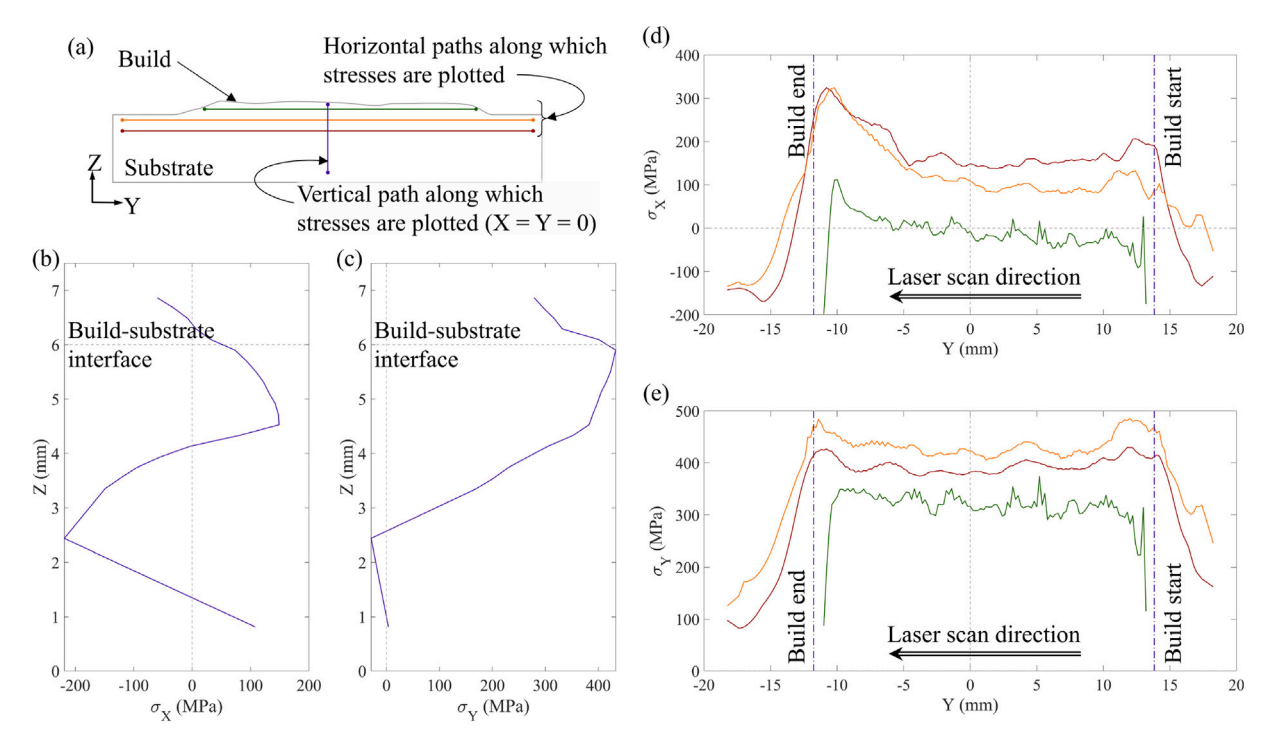


Fig. 11. (a) Illustration of linear paths within the single-layer samples along which stresses are plotted. (b, c) Distribution of σ_X and σ_Y along path X = Y = 0. (d, e) Distribution of σ_X and σ_Y along the various horizontal paths.

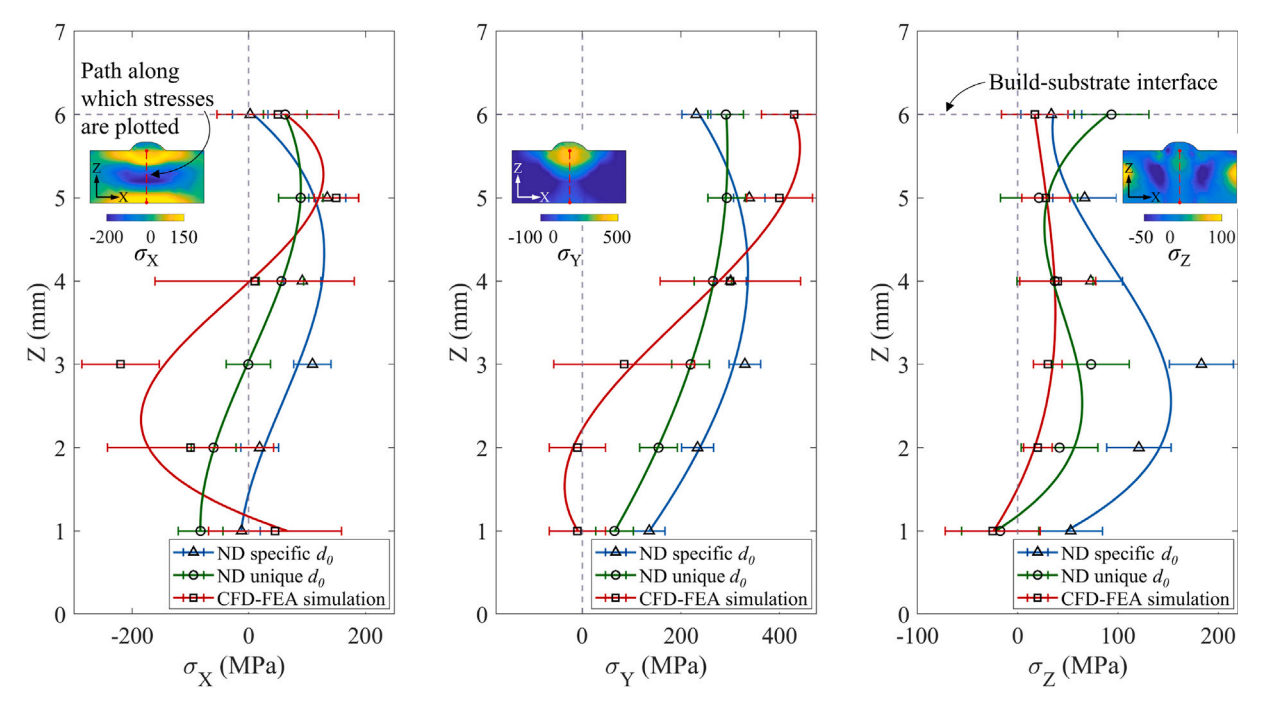


Fig. 12. Comparison of two ND RS measurement methods and that predicted via the one-way coupled thermofluidic-thermomechanical framework at the end of deposition of the first layer. Note that the ND measurement points shown by triangle and circle markers, and predicted gage-volume-averaged points shown by square markers represent the actual magnitudes after calculation, whereas the curves are 3rd degree polynomial fits to the said points. Error bars on the predicted profiles represent 95% confidence intervals of variation of stress within the gage volume. Inset plots depict the path along which stresses are plotted.

component σ_X . Fig. 11(e) also shows that σ_Y is greatest near the buildsubstrate interface (\sim Z = 5.5 mm). Given that a Gaussian heat source is considered for the thermofluidic model, when considering the temporal heat distribution observed in the thermomechanical model, a double ellipsoidal temperature (and heat) distribution pattern is revealed as seen earlier in Fig. 9. This is similar to the observations made earlier by Goldak et al. [39]. As a result of the direction and movement of the double ellipsoidal heat affected zone (HAZ), the normal components of RS transition from tensile to compressive along the depth in very different ways. The $\sigma_{\rm Y}$ component gradually transitions from high tensile to low compressive stress magnitudes when going deeper beneath the build-surface, yet the $\sigma_{\rm V}$ component reveals a much sharper transition to higher magnitude compressive stress at relatively shallower depths beneath the build surface. This presence of tensile and compressive RS is clearly necessary to attain force equilibrium within the specimen. The very low magnitude of $\sigma_{\rm X}$ within the DED build is due to a near plane-stress condition, while $\sigma_{\rm Y}$ is highly tensile due to resistance to the thermal contraction during cooling. The longitudinal distribution of RS presented in Fig. 11(d) and (e) is relatively uniform in the region Y =-5 mm to 5 mm, representing a pseudo-steady-state condition during the build. Beyond these limits, there is an increase in tensile RS in both X and Y components plausibly due to factors like edge geometry stress concentration, direct laser heating of the substrate, and/or other artifacts like porosities/voids. Similar to the observations made from Fig. 11(b) and (c), σ_Y reveals a transition beyond the build region to relatively low magnitudes of tensile RS, whereas, σ_X reveals a transition beyond the build region to compressive RS. The increased magnitude of RS observed at the end of the build (compared to the start of the build) is due to larger thermal gradient (faster cooling) at the end, after the laser heat source has been switched off.

To compare numerically predicted RS with experimentally determined RS (via ND), Fig. 12 shows the depthwise (Z direction) RS profiles within the single-layer sample. The ND measured RS values obtained using specific d_0 values for each measurement location are plotted in Fig. 12 as triangle markers with error bars (blue), whereas

the ND measured RS values obtained using only a single unique d_0 for the whole sample are plotted as circle markers with error bars (green). To obtain a one-to-one comparison, the predicted result is also averaged within the corresponding ND gage volume at each location before plotting with square markers along with *error bars* (red). Note that the error bars for the predicted values indicate 95% confidence intervals for the variation of stress within the gage volume. For all three cases, smooth lines connecting the points are 3rd degree polynomial fits to the points. 3rd degree fits are chosen based on the predicted depthwise RS profile shown in Fig. 11(b) and (c) wherein two inflection points are observed. Consequently, the lines themselves do not represent the exact stress profile within the build, but rather, they act as trend lines to improve visual discernibility. A quantitative comparison between the three RS profiles is provided in Table 6, wherein, the root mean square deviation (RMSD) for $\sigma_{\rm X}$, $\sigma_{\rm Y}$ and $\sigma_{\rm Z}$ is given.

Firstly, note that the variation between ND RS obtained using location-specific d_0 calibration samples and that obtained using the single unique d_0 indicates that the material undergoes significant chemical alteration during the DED process (similar to findings in earlier work [30]), caused due to solid phase change and/or impurity-induced defects, resulting in an RMSD of ~71.1 MPa with a maximum variation of ~110 MPa in measured RS. Also, note that the RMSD values for $\sigma_{\rm X}$, $\sigma_{\rm Y}$ and $\sigma_{\rm Z}$ in the last column of Table 6, appear very similar with magnitudes of the variation on the order of tens of kPA. This reveals that there is a relatively uniform influence of chemical alteration across all three normal components of stress, which is to be expected.

Secondly, for all three normal components of RS, the RMSD between the numerical prediction and the measurement via single unique d_0 is less than the RMSD using the location-specific d_0 values. This is also expected since the one-way coupled thermofluidic–thermomechanical model in this work does not account for any chemical alteration of the material during deposition. Accordingly, an average of about 50 MPa of variation (difference between first and second columns in Table 6) can be attributed to chemical alteration of the material. Additionally, the unknown state of RS within the hot-formed substrate, generated

Table 6
Root mean square deviation (RMSD) between prediction and two measurement methods of RS for the single-layer build.

		Prediction vs. unique d_0	Prediction vs. specific d_0	Unique d_0 vs. specific d_0
	σ_{X}	109.460	149.987	71.064
RMSD (MPa)	$\sigma_{ m Y}$	117.516	175.106	71.098
	$\sigma_{ m Z}$	37.236	84.293	71.075

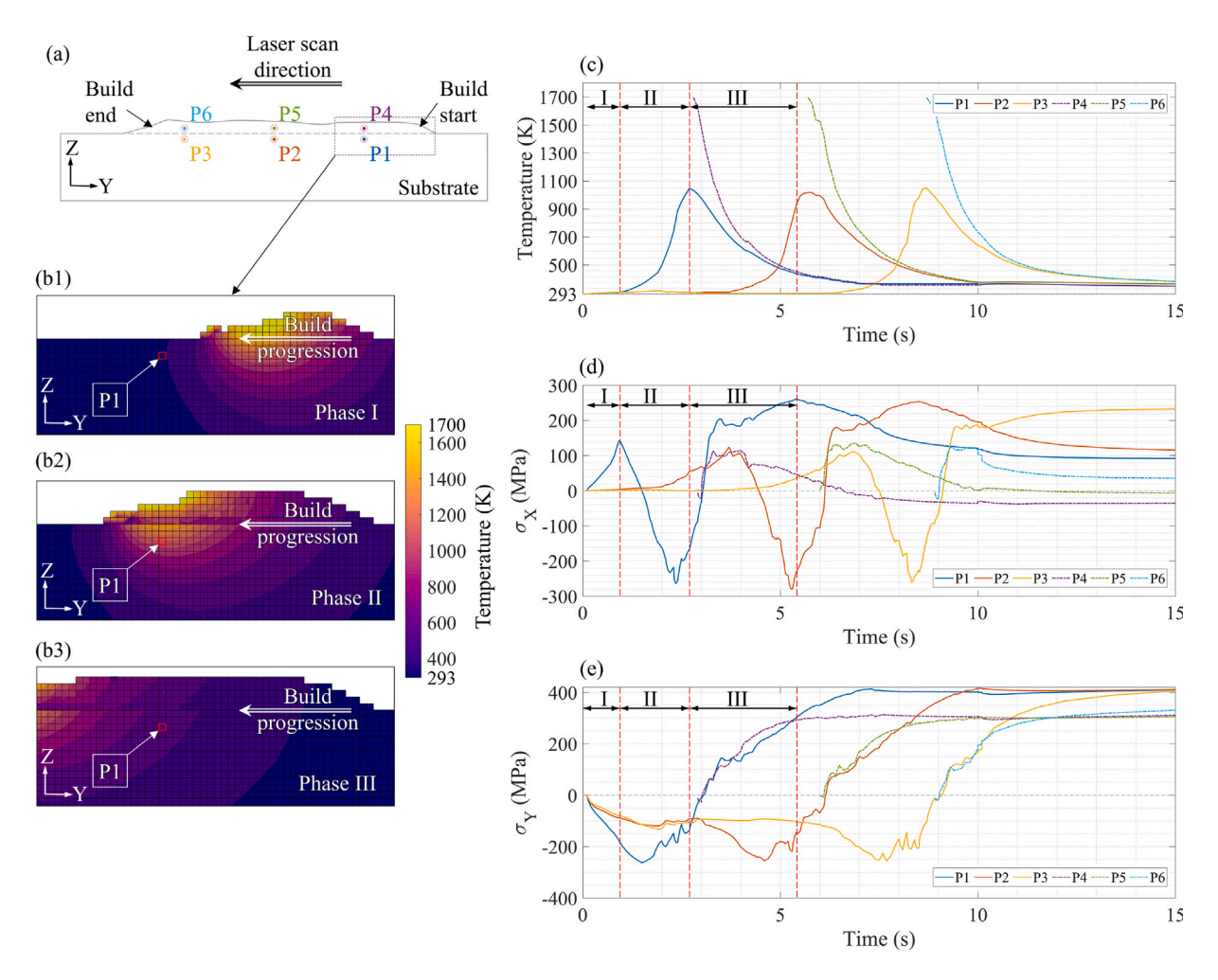


Fig. 13. Temporal evolution of σ_X (d) and σ_Y (e) at locations shown in (a), during deposition of the first layer. (b1) through (b3) illustrate the three phases a point experiences during the printing process. (c) shows the variation of temperature during deposition at the above-mentioned locations.

during its manufacturing process, before DED will influence the final state of RS. Since the numerical model assumes a stress-free substrate, however, this is another potentially significant source of error. It is important to note, however, that the computational framework is fully capable of incorporating an inherent residual stress field within the substrate, as obtained either from experimental measurements or via numerical simulation of the manufacturing process used to produce the substrate. Discrete measurements of inherent RS distribution within the substrate can be readily incorporated in this framework using the iterative stress reconstruction algorithm (ISRA) to ensure a fully compatible and equilibrated state of stress, as demonstrated in earlier work by both the Mathews et al. [78] and Sunny et al. [79]. Moreover, note also that, as seen in Fig. 12, the numerically predicted RS agrees better with experiments in the region Z > 4 mm, as compared to Z <4 mm. This corresponds to regions of fine and coarse meshes in the model, respectively. Although there exists obvious variation between

the trend lines, it should be noted that the polynomial fits are extremely sensitive to changes in individual data points. Consequently, relatively small differences in predicted and measured stresses may manifest as significantly larger variations in the trend lines. In addition, the average experimental error in measured RS magnitude is ~40 MPa, here. This large experimental error is attributed to variations in the microstructure through the build and substrate regions as well as the relatively large gage volume (~1 mm³). Despite the foregoing considerations, the variation between the numerically predicted RS and the experimentally measured RS is within the same order of magnitude as the variation between the two experimental approaches taken for the ND measurement (i.e., unique and location-specific d_0 methods). Consequently, the general trend and relative magnitudes of predicted RS are considered reasonably accurate for providing important insights into the development of RS within AM builds. The evolution of RS during deposition of the first DED layer is illustrated in Fig. 13, and

Fig. 14. Equivalent plastic strain ($\epsilon_{p,eq}$) spatial distribution predicted at the end of deposition of the first layer along the transverse midplane. Inset plot depicts Section B-B on a DED sample

is discussed next. As a preface to this discussion, note that a detailed evolution of RS during metal AM is scarcely found in the existing literature.

The evolution of σ_X and σ_Y at three points within the build and three points directly beneath these in the substrate are plotted as a function of time, in Fig. 13(d) and (e). The locations of the six points (P1 through P6) are shown in Fig. 13(a). Also, Fig. 13 (b1) - (b3) show enlarged views of point P1 at three phases in the deposition process. Phase I is the pre-heating phase where the point under observation does not undergo significant increase in temperature, but where reaction stresses are generated due to heating (from deposition), and consequently thermal expansion of material in the proximity of the point. Phase II, or the deposition phase, initiates when the temperature of the point starts to increase rapidly. During this phase, large compressive stresses are developed due to resistance to thermal expansion. Consequently, for $\sigma_{\rm X}$ tensile reaction stresses are developed in regions ahead of the deposition, whereas relatively small magnitudes of compressive stress are observed for $\sigma_{\rm Y}$. In this period, molten material is deposited on the free surface above P1. Although material is added, it does not participate in stress development until it solidifies (assuming the influence of viscosity, Marangoni flow, and weight of molten medium on stress is negligible). Phase III quickly follows as the laser heat source and deposition move farther away, and the region (containing P1 and P4) undergoes cooling via heat dissipation to the surroundings. During this period, tensile stress develops due to thermal contraction before finally reaching steady-state conditions. The variation of temperatures at points P1 through P6 during the deposition process is shown in Fig. 13(c), depicting the three aforementioned phases for points P1 and P4. These different phases and their corresponding evolution of $\sigma_{\rm X}$ and $\sigma_{\rm V}$ are plotted in Fig. 13(d) and (e), respectively. Note also that the three phases depicted in the figure correspond only to points P1 and P4. Nevertheless, P2 and P5, as well as P3 and P6, also experience similar thermal and mechanical evolution. In the transverse component of RS ($\sigma_{\rm X}$), three inflection points can be observed, corresponding to the three phases mentioned above. In contrast, only two inflection points are present in the longitudinal component of RS ($\sigma_{\rm V}$). This is due to larger influence of reaction stresses in the transverse direction (X) of the build compared to the longitudinal direction (Y). For σ_X , the final inflection point (at $t = \sim 5.5$ s for P1) is a result of reaction stresses developed due to material addition in regions beyond the observation point.

Points located within the build (P4 through P6) only start accumulating normal stress from the instant it solidifies, following which the stress at these points progresses along a similar trend observed for points directly beneath them. Accordingly, the RS evolution lines that contain P4 through P6 only appear in the plot at their respective time of solidification. In the build region, magnitudes of RS developed are lower than those within the substrate due to the relatively lower resistance to thermal expansion/contraction as well as a near plane-stress condition. In summary, the RS developed depends on the rate of change of temperature and resistance to thermal expansion/contraction.

Fig. 14 illustrates the equivalent plastic strain $(\epsilon_{p,eq})$ along the transverse midplane at the end of deposition of the first layer. Inclusion

of Johnson–Cook plasticity in the thermomechanical model reveals development of significant plastic strain, contrary to assumptions in the existing literature [31]. Peak equivalent plastic strain of \sim 0.061 is observed along the build-substrate interface due to the build-up of stress in this region. Plastic strain is revealed in the entire bead as well as notably into the substrate.

Simulating deposition of the second layer, atop the first layer, enables prediction of the evolution of RS from the pre-existing state at the end of printing the first layer. Here, the predicted RS at the end of the deposition for the first layer is specified as an initial condition for the second-layer deposition.

Fig. 15 shows the spatial distribution of von Mises stress along the longitudinal and transverse midplanes, Sections A-A and B-B respectively. The longitudinal stress concentration region is shifted up (in the Z direction) compared to the stress distribution at the end of the first layer (ref. Fig. 10). The peak magnitude of stress is approximately the same as that observed at the end of the first layer, however, the distributed region is expectedly larger. Additionally, there is a concentration of stress at the left side edge of the bead (in Fig. 15, the point at which deposition begins). This is due to direct laser heating of the region before the second layer's material deposition starts. The distribution of transverse and longitudinal normal components of stress along various longitudinal paths in addition to a vertical path on the transverse midplane, at the end of printing the second layer, is quantitatively depicted in Fig. 16. These stress profiles reveal a peak longitudinal component of stress of ~400 MPa within the build. The large amount of variation on the upper-most path (purple horizontal line in Fig. 16(a)) is due to the irregular free surface at the top of the

The ND RS measurements performed on the double-layer sample along the vertical path (X = Y = 0) within the sample, analogous to that of the single-layer case discussed earlier, as well as its comparison with the numerically predicted RS profile, are presented in Fig. 17. The reader is reminded that each ND measurement represents an aggregate reading with a ~1 mm³ gage volume. Similarly, the numerically predicted RS readings are also averaged within a 1 mm³ gage volume. A quantitative comparison of the RS obtained via the two ND calibration approaches with the numerical prediction is presented in Table 7. Due to the increased influence of laser heating, material addition and thermal gradients, the RMSD between ND measurements via both the single unique d_0 and location-specific d_0 are larger as compared to the singlelayer build. Similar to the single-layer build, the numerical prediction agrees better with ND measurement via unique d_0 . The RMSD between the model prediction and the measurement via unique d_0 is reduced in comparison to the single-layer case. This can be attributed to a reduced influence of inherent RS within the substrate during deposition of the second layer. Indeed, recall that for the first layer the inherent RS in the substrate was presumed to be zero in the numerical model, however, there may indeed be a RS field in the substrate which influences the RS after deposition of the first layer. When depositing the second layer, the model does consider the pre-existing inherent RS generated during deposition of the first layer, and hence the RMSD between numerically predicted RS and that determined via ND for the second

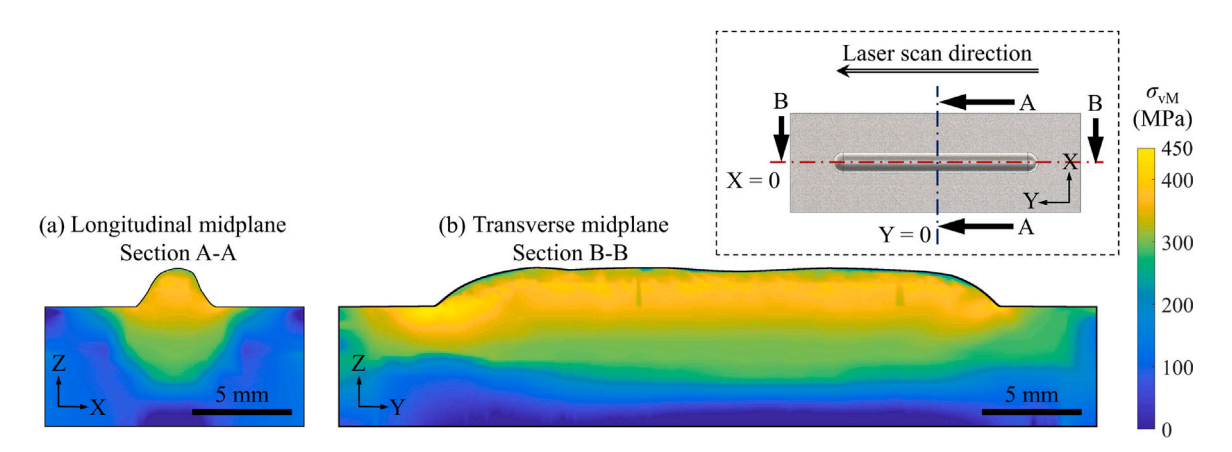


Fig. 15. Von-Mises stress spatial distribution predicted at the end of deposition of the second layer along the longitudinal and transverse midplanes. Inset plot depicts Section A-A and B-B on a DED sample.

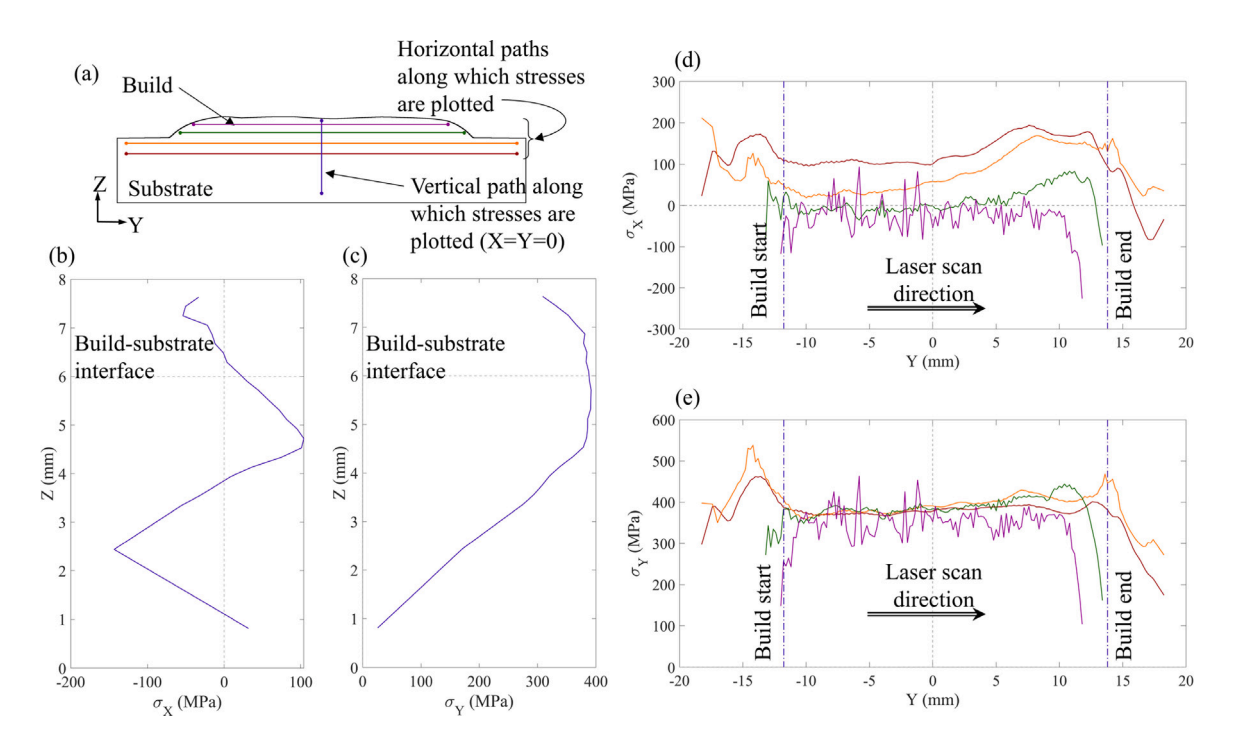


Fig. 16. (a) Illustration of linear paths within the double-layer samples along which stresses are plotted. (b, c) Distribution of σ_X and σ_Y along path X = Y = 0. (d, e) Distribution of σ_X and σ_Y along the various horizontal paths.

layer is relatively lower. Interestingly, the RMSD between prediction and measurement with the location-specific d_0 is smaller compared to the single-layer build. This is plausibly due to chemical changes being manifested as variations in RS, the influence of which is reduced when simulating multiple layers of deposition. Therefore, for builds with several layers, it might be adequate to assume negligible material property change due to chemical alteration during modeling of metal AM.

Due to the structural and thermal evolution in the build during deposition of the second layer, RS in the material also evolves from the inherent RS distributed within the first layer. To observe this evolution, Fig. 18 presents the temporal variation of RS during deposition of the second layer. In Fig. 18, (a) shows the locations of points at which

the evolution of stress is plotted as a function of time in figures (c) and (d). Fig. 18 (b1) - (b3) show the temperature distribution at time instants within the three phases during deposition. Herein, points P6 and P3 follow similar trajectories where the magnitude of stress starts from a non-zero value (from previous deposition), and evolves during heating, deposition, and cooling phases. A repeating pattern is observed in points P5 and P2, as well as in P4 and P1. The evolution profiles are more erratic compared to those of the first layer due to the initial RS. Contrary to the first layer, points P4 through P6 participate in RS evolution during the entire deposition process of the second layer. At the end of deposition, the RS reaches a steady-state tensile condition for both $\sigma_{\rm X}$ and $\sigma_{\rm Y}$.

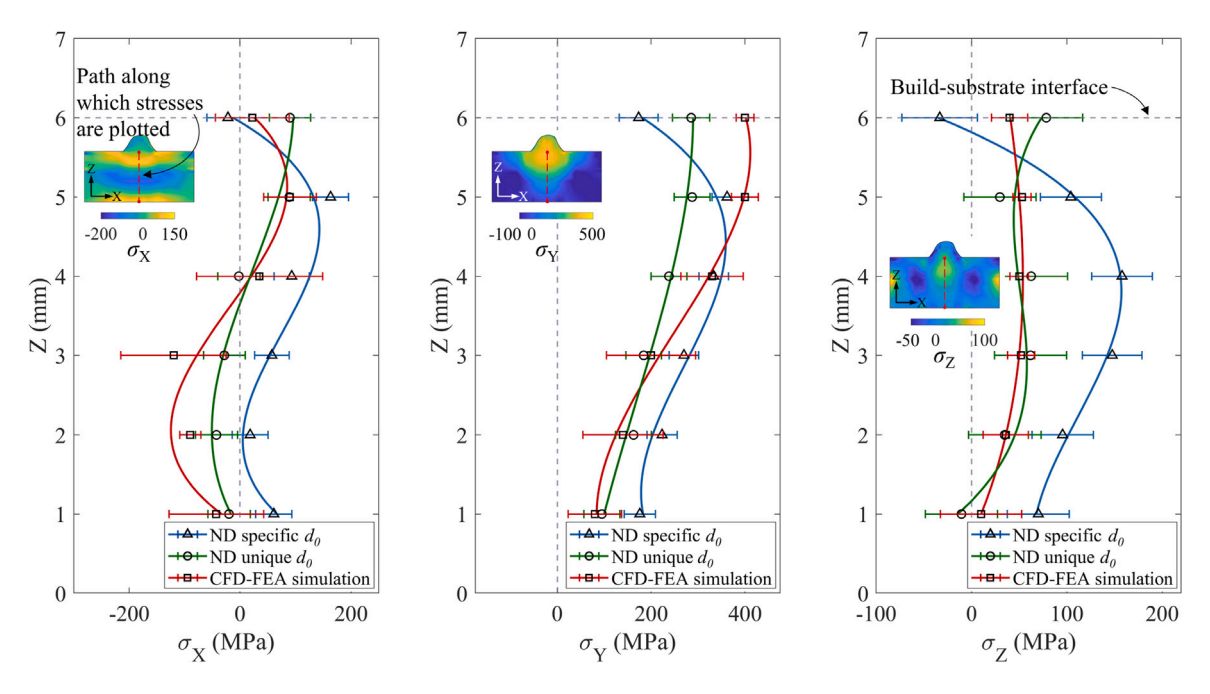


Fig. 17. Comparison of two ND RS measurement methods and that predicted via the one-way coupled thermofluidic-thermomechanical framework at the end of deposition of the second layer. Note that the ND measurement points shown by triangle and circle markers, and predicted gage-volume-averaged points shown by square markers represent the actual magnitudes after calculation, whereas the curves are 3rd degree polynomial fits to the said points. Error bars on the predicted profiles represent 95% confidence intervals of variation of stress within the gage volume. Inset plots depict the path along which stresses are plotted.

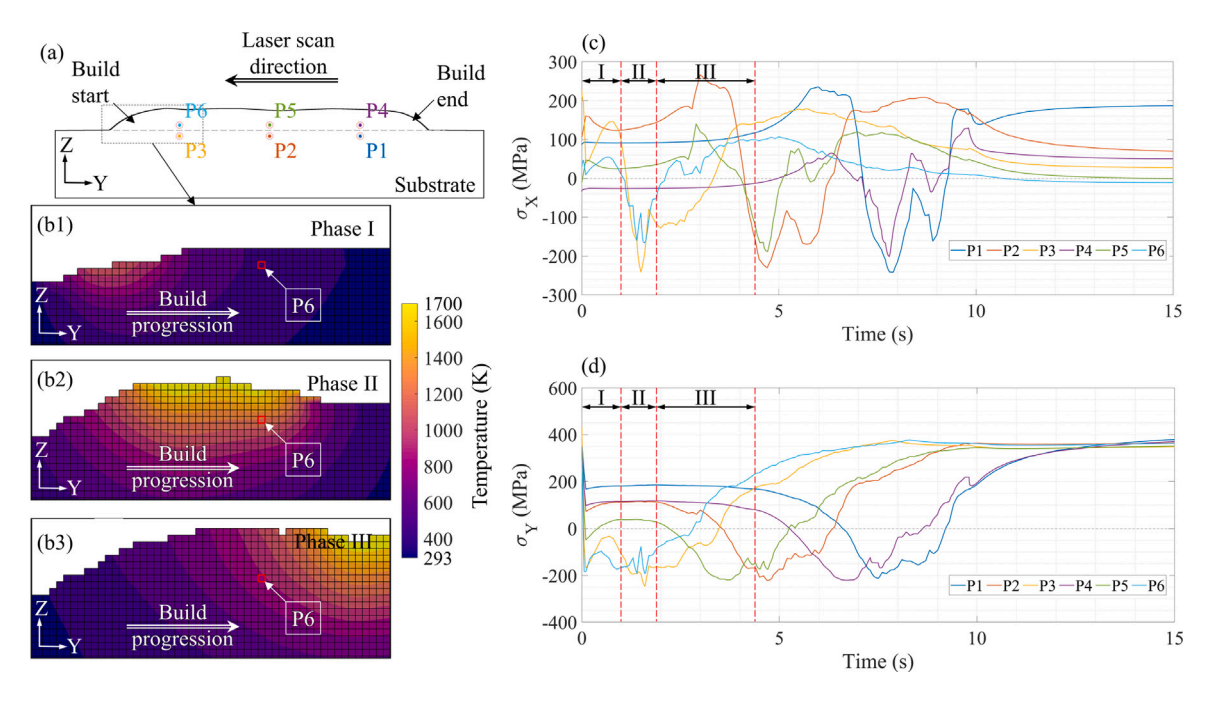


Fig. 18. Temporal evolution of (c) σ_X and (d) σ_Y at locations shown in (a), during deposition of the second layer. (b1) through (b3) illustrate the three phases a point experiences during the printing process.

Table 7Root mean square deviation (RMSD) between prediction and two measurement methods of RS for the double-layer build.

		Prediction vs. unique d_0	Prediction vs. specific d_0	Unique d_0 vs. specific d_0
	σ_{X}	53.562	103.757	86.281
RMSD (MPa)	$\sigma_{ m Y}$	76.669	110.938	86.318
	σ_{Z}	21.216	77.387	86.285

5. Conclusions

A temporally continuous, one-way coupled thermofluidic-thermomechanical framework to model metal additive manufacturing (AM) processes is demonstrated in this work. The computational fluid dynamics (CFD) and finite element analysis (FEA) formulations are linked to simulate powder-based directed energy deposition (DED) of stainless steel (SS) 316L. By establishing a continuous coupling in time. the framework illustrates its capability to predict the evolutions of geometric, thermal, and mechanical behavior during metal AM. The coupling is carried out by mapping both the temperature distribution and surface morphology predicted via the thermofluidic model at progressive instants of time into the thermomechanical model. The residual stress (RS) that manifests in the thermomechanical model upon achieving a state of equilibrium constitutes the initial condition for the temperature and surface morphology that is mapped at the subsequent time step. In effect, the evolution of geometry, temperature, and RS is obtained without making any of the simplifications seen in the prior art to facilitate viable heat source modeling. Contrary to some previously published investigations, this work demonstrates that the inclusion of material plasticity reveals significant plastic flow of the printed material, restricting RS build-up to magnitudes below the yield strength of the material. Moreover, the thermal and RS evolution within arbitrary AM components having highly non-linear geometries can also be predicted with relative ease using the presented method.

Experimental validation of the modeling framework has been demonstrated using single-bead, single- and double-layer DED samples, that are subject to post-build optical 3D surface scanning and X-ray μ CT, to respectively obtain the build surface topography, and information on internal defects. Furthermore, neutron diffraction (ND) RS measurements are performed at several locations within both samples. Comparison of the experimentally acquired data against the demonstrated framework's predictions reveals general overall agreement. Observed are maximum variations of 4.12% between the 3D surface scan and thermofluidic model for the cross-sectional geometry criteria, and ~175 MPa between the ND measurement of RS and its prediction by the one-way coupled thermofluidic-thermomechanical model.

Note that existing experimental techniques such as X-ray diffraction, ND, slitting, etc., readily allow researchers to study the final state of RS in AM components, yet the current technology makes it practically infeasible to study RS evolution over the course of the AM process. Thus the demonstrated modeling framework is particularly useful since

it provides rich "in-situ" information during the material deposition process. Moreover, the framework is readily extensible to other metal AM processes, such as selective laser melting/sintering, electron beam melting, and wire arc AM, among others.

CRediT authorship contribution statement

Ritin Mathews: Conceptualization, Methodology, Formal analysis, Investigation, Data curation, Writing, Visualization. Kishore Mysore Nagaraja: Methodology, Data curation, Writing, Visualization. Runyu Zhang: Methodology, Data curation, Visualization. Sumair Sunny: Conceptualization, Methodology, Visualization, Writing. Haoliang Yu: Conceptualization, Methodology, Visualization, Writing. Deon Marais: Methodology, Data curation. Andrew Venter: Methodology, Data curation. Wei Li: Software, Resources, Writing, Supervision, Project administration. Hongbing Lu: Resources, Methodology. Arif Malik: Software, Resources, Writing, Supervision, Project administration.

Declaration of competing interest

The authors declare that they have no known competing financial interests or personal relationships that could have appeared to influence the work reported in this paper.

Data availability

Data will be made available on request.

Acknowledgments

R. Zhang and H. Lu acknowledge the support of NSF 2219347 and 1726435, and the Department of Energy, USA under DE-NA0003962 and DE-NA0003525. Access and user support for the MPISI instrument are acknowledged.

Appendix A. X-ray micro computed tomography (µct)

A Nikon 225 kV X-ray μ CT system is used to inspect the interior and surface profile of the builds. The system is composed of a Nikon Microfocus 225 kV X-ray source, a moving stage, and an X-ray digital detector, as shown in Fig. A.19. All the movements are controlled remotely either by computer software or through the machine's console.

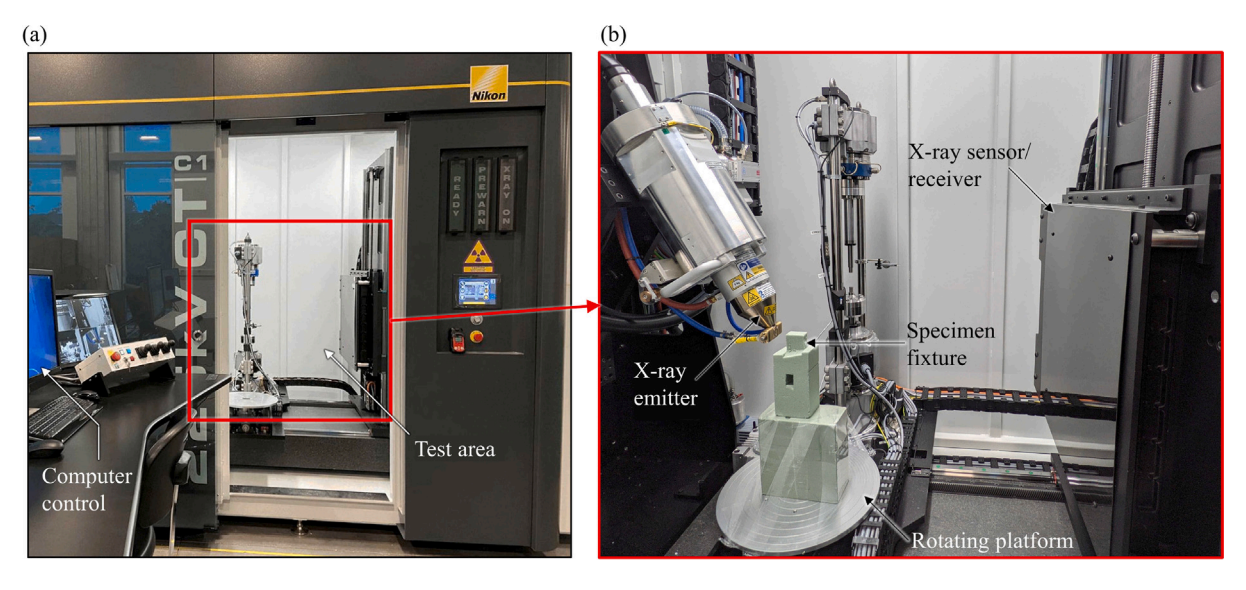


Fig. A.19. Photograph of the X-ray micro computed tomography (μ CT) machine used in this work.

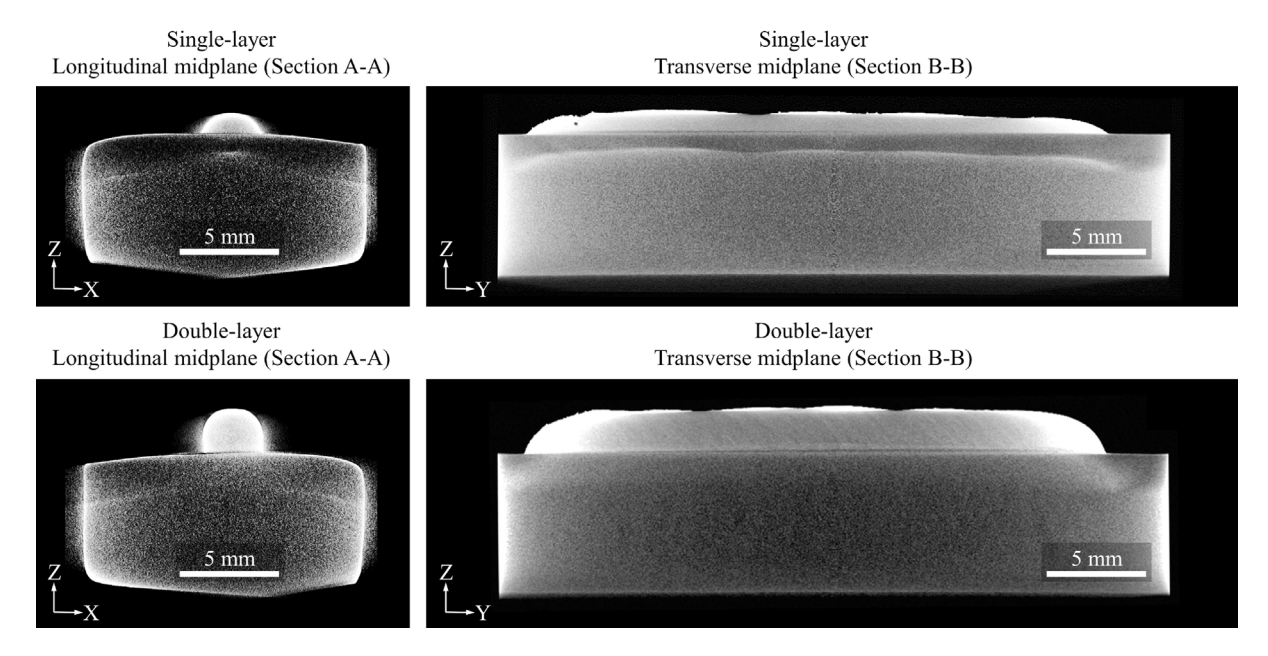


Fig. A.20. X-ray µCT reconstruction results along Section A-A (Left) and B-B (Right) (refer Fig. 2) for both single-layer (Top) and double-layer (Bottom) samples.

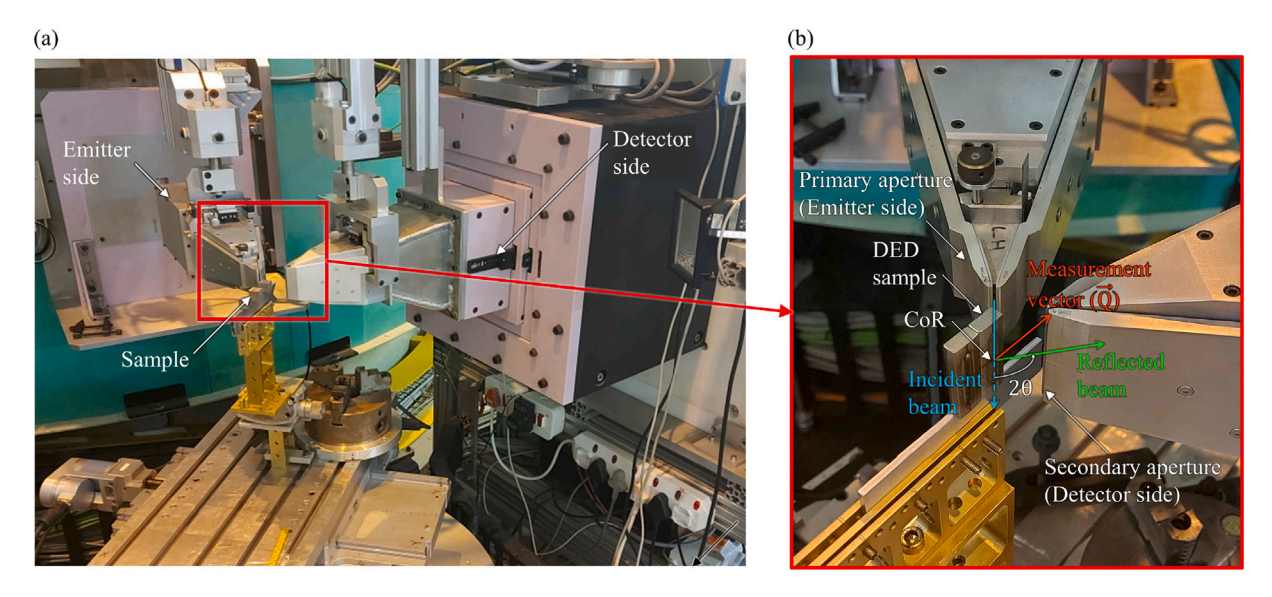


Fig. B.21. (a) Photograph of the MPISI neutron diffractometer setup at the SAFARI-1 research reactor [60]. (b) Enlarged view of the primary and secondary apertures, depicting the paths of the incident beam, diffracted/reflected beam, and the measurement vector, \vec{Q} . Note that all three vectors lie on the same horizontal plane.

The sample is mounted on the stage, directly in the path of X-ray travel. A portion of X-rays that pass through the sample is absorbed, depending on the material density and thickness, which reduces the amount of X-rays that falls on the detector. The spatial variation in intensity at the detector forms a projection image of the sample. Many such images are obtained by rotating the sample about its centroid. Subsequently, Nikon's computer software reconstructs these projection images into a 3D volumetric image. The volumetric data can be sliced along different planes to analyze interior features of the sample.

Section images along the center planes of both the single and double-layer samples are shown in Fig. A.20. Images in this study have a pixel size of 17.947 μm , acquired using a scanning energy level of 185 kV at 62 μA current. A porosity defect is observed in the single-layer sample transverse midplane (Section B-B) at the left end of the build (end of the deposition process).

Appendix B. Neutron diffraction technique

Fig. B.21 shows the Materials Probe for Industrial Strain Investigations (MPISI) neutron diffraction setup. The neutron beam generated in the reactor, that travel through the primary aperture (emitter side), is reflected about material lattice planes and passes through the secondary aperture (detector side), before being absorbed at the detector. Fig. B.21(b) shows the paths of the incident and reflected beams and the measurement vector, \vec{Q} , that bisects the incident and reflected beams. \vec{Q} represents the component of lattice spacing being measured

Fig. B.22 shows a schematic of the neutron diffraction/reflection phenomenon (Bragg's diffraction). The net change in direction between the incident and reflected beams, 20, is obtained by rotating the secondary aperture about the center of rotation (CoR) i.e., the centroid of the measurement gage volume located within the sample. A distribution of the detected neutron count with respect to the secondary aperture angle is obtained by performing measurements at various

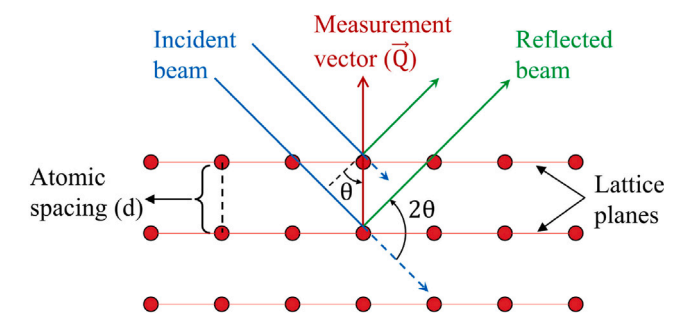


Fig. B.22. Schematic of Bragg's diffraction process used for measuring material lattice spacing.

angles. Subsequently, a Gaussian fit to the data is used to obtain 2θ , the angle at which peak magnitude is observed. Lattice spacing, d, is then calculated using Eq. (B.1).

$$n\lambda = 2d\sin\theta \tag{B.1}$$

where n and λ are the known neutron beam order and wavelength, respectively.

References

- [1] Molitch-Hou M. Overview of additive manufacturing process. In: Additive manufacturing. Elsevier; 2018, p. 1–38. http://dx.doi.org/10.1016/B978-0-12-812155-9.00001-3.
- [2] Ghasri-Khouzani M, Peng H, Rogge R, Attardo R, Ostiguy P, Neidig J, et al. Experimental measurement of residual stress and distortion in additively manufactured stainless steel components with various dimensions. Mater Sci Eng A 2017;707:689–700. http://dx.doi.org/10.1016/j.msea.2017.09.108.
- [3] Song X, Feih S, Zhai W, Sun C-N, Li F, Maiti R, et al. Advances in additive manufacturing process simulation: Residual stresses and distortion predictions in complex metallic components. Mater Des 2020;193:108779. http://dx.doi.org/ 10.1016/j.matdes.2020.108779.
- [4] Gu DD, Meiners W, Wissenbach K, Poprawe R. Laser additive manufacturing of metallic components: materials, processes and mechanisms. Int Mater Rev 2012;57(3):133–64. http://dx.doi.org/10.1179/1743280411Y.0000000014.
- [5] Dass A, Moridi A. State of the art in directed energy deposition: From additive manufacturing to materials design. Coatings 2019;9(7):418. http://dx.doi.org/10. 3390/coatings9070418.
- [6] Bussu G, Irving P. The role of residual stress and heat affected zone properties on fatigue crack propagation in friction stir welded 2024-T351 aluminium joints. Int J Fatigue 2003;25(1):77–88. http://dx.doi.org/10.1016/S0142-1123(02)00038-
- [7] Zhang J, Wang X, Paddea S, Zhang X. Fatigue crack propagation behaviour in wire+ arc additive manufactured Ti-6Al-4V: Effects of microstructure and residual stress. Mater Des 2016;90:551-61. http://dx.doi.org/10.1016/j.matdes. 2015.10.141.
- [8] Advancing aerospace development with metal 3D printing technology and post-processing. 2021, GE Additive Webinar (2021), URL https://event.on24.com/wcc/r/2995356/247492E763F0BC54481579821E5E7E7D?.
- [9] Blakey-Milner B, Gradl P, Snedden G, Brooks M, Pitot J, Lopez E, et al. Metal additive manufacturing in aerospace: A review. Mater Des 2021;209:110008. http://dx.doi.org/10.1016/j.matdes.2021.110008.
- [10] Zitelli C, Folgarait P, Di Schino A. Laser powder bed fusion of stainless steel grades: a review. Metals 2019;9(7):731. http://dx.doi.org/10.3390/met9070731.
- [11] Manfredi D, Bidulskỳ R. Laser powder bed fusion of aluminum alloys. Acta Metall Slovaca 2017;23(3):276–82. http://dx.doi.org/10.12776/ams.v23i3.988.
- [12] Eskandari Sabzi H. Powder bed fusion additive layer manufacturing of titanium alloys. Mater Sci Technol 2019;35(8):875–90. http://dx.doi.org/10.1080/ 02670836.2019.1602974.
- [13] Tian Z, Zhang C, Wang D, Liu W, Fang X, Wellmann D, et al. A review on laser powder bed fusion of inconel 625 nickel-based alloy. Appl Sci 2019;10(1):81. http://dx.doi.org/10.3390/app10010081.
- [14] Wei H, Mukherjee T, Zhang W, Zuback J, Knapp G, De A, et al. Mechanistic models for additive manufacturing of metallic components. Prog Mater Sci 2021;116:100703. http://dx.doi.org/10.1016/j.pmatsci.2020.100703.
- [15] Sochalski-Kolbus L, Payzant EA, Cornwell PA, Watkins TR, Babu SS, Dehoff RR, et al. Comparison of residual stresses in Inconel 718 simple parts made by electron beam melting and direct laser metal sintering. Metall Mater Trans A 2015;46:1419–32. http://dx.doi.org/10.1007/s11661-014-2722-2.

- [16] Rangaswamy P, Griffith M, Prime M, Holden T, Rogge R, Edwards J, et al. Residual stresses in LENS® components using neutron diffraction and contour method. Mater Sci Eng A 2005;399(1–2):72–83. http://dx.doi.org/10.1016/j. msea.2005.02.019.
- [17] Weisz-Patrault D, Margerit P, Constantinescu A. Residual stresses in thin walled-structures manufactured by directed energy deposition: In-situ measurements, fast thermo-mechanical simulation and buckling. Addit Manuf 2022;56:102903. http://dx.doi.org/10.1016/j.addma.2022.102903.
- [18] Liao S, Webster S, Huang D, Council R, Ehmann K, Cao J. Simulation-guided variable laser power design for melt pool depth control in directed energy deposition. Addit Manuf 2022;56:102912. http://dx.doi.org/10.1016/j.addma. 2022.102912.
- [19] Menon N, Mondal S, Basak A. Multi-fidelity surrogate-based process mapping with uncertainty quantification in laser directed energy deposition. Materials 2022;15(8):2902. http://dx.doi.org/10.3390/ma15082902.
- [20] Vastola G, Zhang G, Pei Q, Zhang Y-W. Controlling of residual stress in additive manufacturing of Ti6Al4V by finite element modeling. Addit Manuf 2016;12:231–9. http://dx.doi.org/10.1016/j.addma.2016.05.010.
- [21] Jihong Z, Han Z, Chuang W, Lu Z, Shangqin Y, Zhang W. A review of topology optimization for additive manufacturing: Status and challenges. Chin J Aeronaut 2021;34(1):91–110. http://dx.doi.org/10.1016/j.cja.2020.09.020.
- [22] Vasinonta A, Beuth JL, Griffith M. Process maps for predicting residual stress and melt pool size in the laser-based fabrication of thin-walled structures. J Manuf Sci Eng 2007;129(1):101–9. http://dx.doi.org/10.1115/1.2335852.
- [23] Meng L, McWilliams B, Jarosinski W, Park H-Y, Jung Y-G, Lee J, et al. Machine learning in additive manufacturing: a review. Jom 2020;72:2363–77. http://dx.doi.org/10.1007/s11837-020-04155-y.
- [24] Jin Z, Zhang Z, Demir K, Gu GX. Machine learning for advanced additive manufacturing. Matter 2020;3(5):1541–56. http://dx.doi.org/10.1016/j.matt.2020.08.
- [25] Perumal V, Abueidda D, Koric S, Kontsos A. Temporal convolutional networks for data-driven thermal modeling of directed energy deposition. J Manuf Process 2023;85:405–16. http://dx.doi.org/10.1016/j.jmapro.2022.11.063.
- [26] Kats D, Wang Z, Gan Z, Liu WK, Wagner GJ, Lian Y. A physics-informed machine learning method for predicting grain structure characteristics in directed energy deposition. Comput Mater Sci 2022;202:110958. http://dx.doi.org/10.1016/j. commatsci.2021.110958.
- [27] Jamshidinia M, Kong F, Kovacevic R. The coupled CFD-FEM model of electron beam melting®(EBM). Citeseer; 2013.
- [28] Cheon J, Kiran DV, Na S-J. Thermal metallurgical analysis of GMA welded AH36 steel using CFD-FEM framework. Mater Des 2016;91:230–41. http://dx.doi.org/ 10.1016/j.matdes.2015.11.099.
- [29] Mukherjee T, Zhang W, DebRoy T. An improved prediction of residual stresses and distortion in additive manufacturing. Comput Mater Sci 2017;126:360–72. http://dx.doi.org/10.1016/j.commatsci.2016.10.003.
- [30] Bailey NS, Katinas C, Shin YC. Laser direct deposition of AISI H13 tool steel powder with numerical modeling of solid phase transformation, hardness, and residual stresses. J Mater Process Technol 2017;247:223–33. http://dx.doi.org/ 10.1016/j.jmatprotec.2017.04.020.
- [31] Chen F, Yan W. High-fidelity modelling of thermal stress for additive manufacturing by linking thermal-fluid and mechanical models. Mater Des 2020;196:109185. http://dx.doi.org/10.1016/j.matdes.2020.109185.
- [32] Beghini LL, Stender M, Moser D, Trembacki BL, Veilleux MG, Ford KR. A coupled fluid-mechanical workflow to simulate the directed energy deposition additive manufacturing process. Comput Mech 2021;67(4):1041–57. http://dx.doi.org/10. 1007/s00466-020-01960-9.
- [33] Liang L, Hu R, Wang J, Huang A, Pang S. A thermal fluid mechanical model of stress evolution for wire feeding-based laser additive manufacturing. J Manuf Process 2021;69:602–12. http://dx.doi.org/10.1016/j.jmapro.2021.08.008.
- [34] Lindgren L-E. Finite element modeling and simulation of welding part 1: increased complexity. J Therm Stresses 2001;24(2):141–92. http://dx.doi.org/ 10.1080/01495730150500442.
- [35] Uriondo A, Esperon-Miguez M, Perinpanayagam S. The present and future of additive manufacturing in the aerospace sector: A review of important aspects. Proc Inst Mech Eng G 2015;229(11):2132–47. http://dx.doi.org/10. 1177/0954410014568797.
- [36] Hussein A, Hao L, Yan C, Everson R. Finite element simulation of the temperature and stress fields in single layers built without-support in selective laser melting. Mater Des (1980-2015) 2013;52:638–47. http://dx.doi.org/10.1016/j.matdes. 2013.05.070.
- [37] Farahmand P, Kovacevic R. An experimental-numerical investigation of heat distribution and stress field in single-and multi-track laser cladding by a highpower direct diode laser. Opt Laser Technol 2014;63:154–68. http://dx.doi.org/ 10.1016/j.optlastec.2014.04.016.
- [38] Heigel J, Michaleris P, Reutzel EW. Thermo-mechanical model development and validation of directed energy deposition additive manufacturing of Ti-6Al-4V. Addit Manuf 2015;5:9-19. http://dx.doi.org/10.1016/j.addma.2014.10.003.
- [39] Goldak J, Chakravarti A, Bibby M. A new finite element model for welding heat sources. Metall Trans B 1984;15(2):299–305. http://dx.doi.org/10.1007/ BF02667333.

- [40] Prabhakar P, Sames WJ, Dehoff R, Babu SS. Computational modeling of residual stress formation during the electron beam melting process for Inconel 718. Addit Manuf 2015;7:83–91. http://dx.doi.org/10.1016/j.addma.2015.03.003.
- [41] Kiran A, Li Y, Hodek J, Brázda M, Urbánek M, Džugan J. Heat source modeling and residual stress analysis for metal directed energy deposition additive manufacturing. Materials 2022;15(7):2545. http://dx.doi.org/10.3390/ ma15072545
- [42] Zhang Y, Zhang J. Finite element simulation and experimental validation of distortion and cracking failure phenomena in direct metal laser sintering fabricated component. Addit Manuf 2017;16:49–57. http://dx.doi.org/10.1016/ i.addma.2017.05.002.
- [43] Li C, Denlinger ER, Gouge MF, Irwin JE, Michaleris P. Numerical verification of an octree mesh coarsening strategy for simulating additive manufacturing processes. Addit Manuf 2019;30:100903. http://dx.doi.org/10.1016/j.addma.2019. 100903
- [44] Tan P, Shen F, Li B, Zhou K. A thermo-metallurgical-mechanical model for selective laser melting of Ti6Al4V. Mater Des 2019;168:107642. http://dx.doi. org/10.1016/j.matdes.2019.107642.
- [45] Nagaraja KM, Li W, Qian D, Vasudevan V, Pyun Y, Lu H. Multiphysics modeling of in situ integration of directed energy deposition with ultrasonic nanocrystal surface modification. Int J Adv Manuf Technol 2022;120(7):5299–310. http: //dx.doi.org/10.1007/s00170-022-09082-7.
- [46] Yao B, Lu X, Ma L, Kang N, Sui S, Tan H, et al. An enhanced finite element modelling based on self-regulation effect in directed energy deposition of Ti–6Al– 4V. J Mater Res Technol 2022;17:1187–99. http://dx.doi.org/10.1016/j.jmrt. 2022.01.079.
- [47] Marangoni C, Stefanelli P, Liceo R. Monografia sulle bolle liquide. Il Nuovo Cimento 1872;7–8(1):301–56. http://dx.doi.org/10.1007/BF02824616.
- [48] Leung CLA, Marussi S, Atwood RC, Towrie M, Withers PJ, Lee PD. In situ X-ray imaging of defect and molten pool dynamics in laser additive manufacturing. Nature Commun 2018;9(1):1–9. http://dx.doi.org/10.1038/s41467-018-03734-7.
- [49] Li W, Kishore M, Zhang R, Bian N, Lu H, Li Y, et al. Comprehensive studies of SS316L/IN718 functionally gradient material fabricated with directed energy deposition: Multi-physics & multi-materials modelling and experimental validation. Addit Manuf 2023;61:103358. http://dx.doi.org/10.1016/j.addma.2022.103358.
- [50] Raghavan A, Wei H, Palmer T, Debroy T. Heat transfer and fluid flow in additive manufacturing. J Lasers Appl 2013;25(5):052006. http://dx.doi.org/10.2351/1. 4817788
- [51] Manvatkar V, De A, DebRoy T. Spatial variation of melt pool geometry, peak temperature and solidification parameters during laser assisted additive manufacturing process. Mater Sci Technol 2015;31(8):924–30. http://dx.doi.org/ 10.1179/1743284714Y.0000000701.
- [52] He X, Mazumder J. Transport phenomena during direct metal deposition. J Appl Phys 2007;101(5):053113. http://dx.doi.org/10.1063/1.2710780.
- [53] Hirt CW, Nichols BD. Volume of fluid (VOF) method for the dynamics of free boundaries. J Comput Phys 1981;39(1):201–25. http://dx.doi.org/10.1016/0021-9991(81)90145-5.
- [54] Körner C, Bauereiß A, Attar E. Fundamental consolidation mechanisms during selective beam melting of powders. Modelling Simul Mater Sci Eng 2013;21(8):085011. http://dx.doi.org/10.1088/0965-0393/21/8/085011.
- [55] Gan Z, Liu H, Li S, He X, Yu G. Modeling of thermal behavior and mass transport in multi-layer laser additive manufacturing of Ni-based alloy on cast iron. Int J Heat Mass Transfer 2017;111:709–22. http://dx.doi.org/10.1016/j. iiheatmasstransfer 2017 04 055.
- [56] Yan W, Qian Y, Ge W, Lin S, Liu WK, Lin F, et al. Meso-scale modeling of multiple-layer fabrication process in selective electron beam melting: interlayer/track voids formation. Mater Des 2018;141:210–9. http://dx.doi.org/10. 1016/j.matdes.2017.12.031.
- [57] Zhang R, Nagaraja KM, Bian N, Fisher E, Ahmadyar S, Bayazitoglu K, et al. Experimental studies on fabricating functionally gradient material of stainless steel 316L-Inconel 718 through hybrid manufacturing: directed energy deposition and machining. Int J Adv Manuf Technol 2022;120(11–12):7815–26. http://dx. doi.org/10.1007/s00170-022-09304-y.
- [58] Mostafaei A, Zhao C, He Y, Ghiaasiaan SR, Shi B, Shao S, et al. Defects and anomalies in powder bed fusion metal additive manufacturing. Curr Opin Solid State Mater Sci 2022;26(2):100974. http://dx.doi.org/10.1016/j.cossms. 2021.100974.

- [59] Koutiri I, Pessard E, Peyre P, Amlou O, De Terris T. Influence of SLM process parameters on the surface finish, porosity rate and fatigue behavior of as-built Inconel 625 parts. J Mater Process Technol 2018;255:536–46. http://dx.doi.org/ 10.1016/j.jmatprotec.2017.12.043.
- [60] Venter AM, van Heerden PR, Marais D, Raaths JC. MPISI: The neutron strain scanner materials probe for internal strain investigations at the SAFARI-1 research reactor. Physica B 2018;551:417–21. http://dx.doi.org/10.1016/j.physb. 2017.12.011.
- [61] Hutchings MT, Withers PJ, Holden TM, Lorentzen T. Introduction to the characterization of residual stress by neutron diffraction. CRC Press; 2005, http://dx.doi.org/10.1201/9780203402818.
- [62] Mills KC. Recommended values of thermophysical properties for selected commercial alloys. Woodhead Publishing; 2002.
- [63] Flow Science, Inc. FLOW-3D, version 12.0. 2019, Santa Fe, NM, URL https://www.flow3d.com/.
- [64] Wen S, Shin Y, Murthy J, Sojka P. Modeling of coaxial powder flow for the laser direct deposition process. Int J Heat Mass Transfer 2009;52(25–26):5867–77. http://dx.doi.org/10.1016/j.ijheatmasstransfer.2009.07.018.
- [65] Lee Y. Simulation of laser additive manufacturing and its applications. The Ohio State University; 2015, URL https://www.proquest.com/dissertations-theses/ simulation-laser-additive-manufacturing/docview/1775393620/se-2.
- [66] Gürtler F-J, Karg M, Leitz K-H, Schmidt M. Simulation of laser beam melting of steel powders using the three-dimensional volume of fluid method. Physics Procedia 2013;41:881–6. http://dx.doi.org/10.1016/j.phpro.2013.03.162.
- [67] Saldi ZS. Marangoni driven free surface flows in liquid weld pools. Citeseer; 2012, http://dx.doi.org/10.4233/uuid:8401374b-9e9c-4d25-86b7-fc445ec73d27.
- [68] Zhang Y, Lim C, Tang C, Li B. Numerical investigation on heat transfer of melt pool and clad generation in directed energy deposition of stainless steel. Int J Therm Sci 2021;165:106954. http://dx.doi.org/10.1016/j.ijthermalsci.2021. 106054
- [69] Indhu R, Vivek V, Sarathkumar L, Bharatish A, Soundarapandian S. Overview of laser absorptivity measurement techniques for material processing. Lasers Manuf Mater Process 2018;5(4):458–81. http://dx.doi.org/10.1007/s40516-018-0075-
- [70] Bergström D. The absorptance of metallic alloys to Nd: YAG and Nd: YLF laser light [Ph.D. thesis], Luleå tekniska universitet; 2005.
- [71] Gao X, Yao X, Niu F, Zhang Z. The influence of nozzle geometry on powder flow behaviors in directed energy deposition additive manufacturing. Adv Powder Technol 2022;33(3):103487. http://dx.doi.org/10.1016/j.apt.2022.103487.
- [72] Kim CS. Thermophysical properties of stainless steels. Tech. Rep., Argonne National Lab., Ill.(USA); 1975, http://dx.doi.org/10.2172/4152287, URL https://www.osti.gov/biblio/4152287.
- [73] Qin Q, Zhang D-t, Zang Y, Guan B. A simulation study on the multipass rolling bond of 316L/Q345R stainless clad plate. Adv Mech Eng 2015;7(7):1687814015594313. http://dx.doi.org/10.1177/1687814015594313.
- [74] Chandrasekaran H, M'saoubi R, Chazal H. Modelling of material flow stress in chip formation process from orthogonal milling and split Hopkinson bar tests. Mach Sci Technol 2005;9(1):131–45. http://dx.doi.org/10.1081/MST-200051380.
- [75] Amidror I. Scattered data interpolation methods for electronic imaging systems: a survey. J Electron Imaging 2002;11(2):157–76. http://dx.doi.org/10.1117/1. 1455013.
- [76] Javaid M, Haleem A, Kumar L. Dimensional errors during scanning of product using 3D scanner. In: Advances in engineering design. Springer; 2019, p. 727–36. http://dx.doi.org/10.1007/978-981-13-6469-3_67.
- [77] Vásárhelyi L, Kónya Z, Kukovecz Á, Vajtai R. Microcomputed tomography-based characterization of advanced materials: a review. Mater Today Adv 2020;8:100084. http://dx.doi.org/10.1016/j.mtadv.2020.100084.
- [78] Mathews R, Sunny S, Malik A, Halley J. Coupling between inherent and machining-induced residual stresses in aluminum components. Int J Mech Sci 2022;213:106865. http://dx.doi.org/10.1016/j.ijmecsci.2021.106865.
- [79] Sunny S, Mathews R, Gleason G, Malik A, Halley J. Effect of metal additive manufacturing residual stress on post-process machining-induced stress and distortion. Int J Mech Sci 2021;202:106534. http://dx.doi.org/10.1016/j.ijmecsci. 2021.106534.